Distinctive behavioural anomalies, structural brain phenotypes and cortical hyper-connectivity in *Chd8*-deficient mice

Philipp Suetterlin[1*], Shaun Hurley[1*], Conor Mohan[1*], Kimberley L. H. Riegman[1*], Angela Caruso[2,3*], Marco Pagani[4], Jacob Ellegood[5], Alberto Galbusera[4], Ivan Crespo-Enriquez[1], Caterina Michetti[2,6], Robert Ellingford[1], Olivier Brock[7], Alessio Delogu[7], Philippa Francis-West[1], Jason P. Lerch[5], Maria Luisa Scattoni[2], Alessandro Gozzi[4], Cathy Fernandes[8,9], & M. Albert Basson[1,9^]

[1]Department of Craniofacial Development and Stem Cell Biology, King's College London, Floor 27, Guy's Hospital Tower Wing, London, SE1 9RT, UK
[2]Neurotoxicology and Neuroendocrinology Section, Department of Cell Biology and Neuroscience, Istituto Superiore di Sanità, Viale Regina Elena 299,00161 Rome, Italy
[3]School of Behavioural Neuroscience, Department of Psychology, Sapienza University of Rome, via dei Marsi 78, 00185, Rome, Italy
[4]Istituto Italiano di Tecnologia, Center for Neuroscience and Cognitive Systems @ UniTn, 38068 Rovereto, TN, Italy
[5]Department of Medical Biophysics, University of Toronto, Mouse Imaging Centre, Hospital for Sick Children, 25 Orde Street, Toronto, Ontario M5T 3H7, Canada
[6]Center for Synaptic Neuroscience and Technology, Istituto Italiano di Tecnologia, Genova, Italy
[7]Department of Basic and Clinical Neuroscience, Institute of Psychiatry, Psychology & Neuroscience, King's College London, UK
[8]MRC Social, Genetic & Developmental Psychiatry Centre, PO82, Institute of Psychiatry, Psychology & Neuroscience, King's College London, De Crespigny Park, London SE5 8AF, UK
[9]MRC Centre for Neurodevelopmental Disorders, King's College London, 4th floor, New Hunt's House, London SE1 1UL, UK

* First co-authors

^Corresponding author

ABSTRACT

Truncating *CHD8* mutations are amongst the highest confidence risk factors for autism spectrum disorders (ASD) identified to date. To investigate how reduced *Chd8* gene dosage may disrupt brain development and predispose individuals to ASD, we generated a *Chd8* heterozygous mouse model. In line with clinical observations, we found that *Chd8* heterozygous mice displayed subtle brain hyperplasia and hypertelorism, coupled with increased postnatal brain weight. *Chd8* heterozygous mice displayed anomalous behaviours, but autism-like social deficits, repetitive and restricted behaviours were not present. Only minor gene expression changes were observed in the embryonic neocortex at E12.5, with more pronounced gene expression changes in postnatal cortex at P5. Differentially expressed genes showed highly significant enrichment for known autism candidates. Amongst the down-regulated transcripts, genes involved in cell adhesion and axon guidance were particularly prominent, implicating impaired connectivity as a potential mechanism underlying the ASD phenotype. To probe this further, we performed resting state functional fMRI and found increased synchronised activity in cortico-hippocampal and auditory-parietal networks, hinting at impaired sensory processing. Together, these data show that *Chd8* heterozygous mice recapitulate key clinical features found in patients with *CHD8* mutations and show a unique combination of behavioural phenotypes, which may be underpinned by a distinctive disruption of brain connectivity and sensory processing.

Autism spectrum disorder (ASD) is diagnosed on the basis of socio-communicative deficits and repetitive, perseverative behaviours with restricted interests (1). The recent identification of de novo, likely gene disrupting (LGD) mutations that show highly significant associations with autism (2-6) provides an opportunity to identify the underlying neurodevelopmental deficits. Several of the highest confidence ASD risk genes identified in these studies encode chromatin remodelling factors (7). A critical question is whether chromatin remodelling deficits converge on known autism-associated pathways, or whether neural development is disrupted in novel ways in ASD subtypes associated with chromatin remodelling factors.

Resting state functional MRI studies in humans with ASD have provided evidence for reduced long-range synchronisation in spontaneous brain activity, consistent with an "under-connectivity" theory of ASD. However, consistent with the heterogeneity of ASD, several different types of rsfMRI abnormalities are potentially present in ASD patients (8), raising the possibility that these could be used in the future as specific biomarkers to stratify the ASD patient population. We recently reported hypo-connectivity of the default mode network, a network that consists of the synchronised spontaneous activation of the frontal, cingulate and retrosplenial cortex, in homozygous Cntnap2 mouse mutants (9).

LGD mutations in *CHD8* (Chromodomain Helicase DNA binding factor 8) are detected exclusively in probands (2-6). Patients with *CHD8* mutations are characterised by a high prevalence of autism, macrocephaly, facial dysmorphisms, motor delay and hypotonia, intellectual disability and gastro-intestinal (GI) problems, and less commonly by anxiety, seizures and hyperactivity (10-13). *CHD8* encodes an ATP-dependent chromatin remodelling protein of the chromodomain helicase DNA binding family (14, 15). CHD8 is recruited to promoters of many actively transcribed genes in mouse and human neural progenitors, with *CHD8* knock-down resulting in downregulation of many autism-associated genes (16, 17). Dysregulation of these pathways may therefore contribute to the autism and macrocephalic

phenotypes associated with human *CHD8* haploinsufficiency. Consistent with this hypothesis, two groups recently reported mild brain overgrowth and autistic-like anomalies in *Chd8*$^{+/-}$ mice, suggesting that *Chd8* heterozygosity may be sufficient to cause these phenotypes (18, 19). However, the behavioural effects reported are subtle, associated with high levels of general anxiety in test animals (18) or not typically associated with ASD (19). More importantly, the molecular and neuroanatomical alterations that may underpin such behavioural phenotypes remain obscure.

In order to address these issues we generated a new Chd8$^{+/-}$ mouse model and asked whether *Chd8* heterozygosity was sufficient to disrupt neurodevelopmental gene expression, brain development and function and cause autism-like behaviours.

We found evidence for accelerated brain growth in Chd8$^{+/-}$ animals, leading to mild megalencephaly in adulthood. Moreover, close inspection of the cranioskeleton revealed hypertelorism reminiscent of the human clinical population. Furthermore, *Chd8* heterozygous mice exhibited a range of behavioural anomalies; however, these didn't include autism-like behaviours, despite significant alterations in brain structure. Interestingly, gene expression in embryonic cortex was only mildly perturbed, with significant changes emerging postnatally. A preferential disruption of transcriptional networks involved in brain wiring and fMRI experiments implicated over-connectivity of cortical sub-cortical networks in the neuropsychiatric disorders caused by *CHD8* haploinsufficiency.

RESULTS

A new mouse line with a conditional *Chd8* allele was produced through homologous recombination in embryonic stem cells (Fig. S1A, B). Cre-mediated deletion of *loxP*-flanked (flox) exon 3 results in an early frameshift and termination of translation at amino acid 419, predicted to produce a protein that lacks all functional domains, equivalent to nonsense and frameshift mutations terminating CHD8 at amino acids 62 and 747 in patients (20). *Chd8*^{flox} mice were crossed with the ubiquitously expressing βactin-Cre line (Fig. S1C) and subsequently back-crossed onto C57Bl6/J to generate Chd8$^{+/-}$ mice.

Quantitative RT-PCR on E12.5 and P5 neocortex confirmed that *Chd8* expression was reduced by 64% (p=0.006, student's t-test) and 52% (p=0.01, student's t-test) respectively (Fig. S1D). This was also true at the protein level, with Western blot experiments on lysates from E12.5 neocortex revealing a 51% reduction in heterozygotes compared to controls (Fig. S1F) with no evidence for the presence of truncated protein products (Fig S1E).

These data validated our *Chd8* heterozygous loss-of-function mouse line as a model for studying *CHD8* haploinsufficiency.

Chd8 heterozygous mice have specific craniofacial and structural brain phenotypes

We asked whether some of the more penetrant human phenotypes associated with *CHD8* haploinsufficiency are recapitulated in *Chd8*$^{+/-}$ mice. Humans with truncating mutations in a single *CHD8* allele have macrocephaly and distinct craniofacial phenotypes, which include hypertelorism (wide-set eyes) (10, 11). Micro-CT analyses showed that the interorbital distance (landmarks 8-9) was significantly wider in *Chd8*$^{+/-}$ mice compared to controls, indicative of a hyperteloric phenotype (Fig. 1C,D,F).

In addition, the anterior-posterior length of the interparietal bone (landmarks 4-5) was increased in *Chd8*$^{+/-}$ animals (Fig. 1E).

To examine whether specific structural brain abnormalities were present in these mice, the brains of *Chd8*$^{+/-}$ mice were compared to *Chd8*$^{+/+}$ mice by high resolution MRI (Fig 1G). Total brain volume was increased by 2.7% in *Chd8*$^{+/-}$ mice (463mm^3 vs 476mm^3, p=0.048, FDR=15%, Fig. 1H). Accordingly, several brain regions that have been implicated in autism (21) – including cortical areas, hippocampus and parts of the cerebellum (Fig. 1G, H, Supplementary Table 1) – showed volumetric increases, providing potential neural substrates for the autism phenotype associated with *CHD8* haploinsufficiency in humans.

Chd8$^{+/-}$ mice exhibit complex behavioural abnormalities not typical of autism mouse models

CHD8 heterozygosity is strongly associated with autism in the human population (2-6). We therefore asked whether *Chd8*$^{+/-}$ mice exhibited any autism-like behavioural abnormalities. *Chd8*$^{+/-}$ mice demonstrated normal social preference in the three-chamber social investigation test, spending significantly more time in the chamber with the unfamiliar conspecific mouse than in the other chambers (Fig. 2A). Interestingly, mutant mice spent slightly more time with the novel mouse than controls (Fig. 2A). Quantifying direct interactions in a reciprocal social interaction test, revealed the same phenotype in mutant mice (Fig. 2B). A quantitative olfactory habituation/dishabituation test also revealed an increased interest in an odour with social significance (urine) in *Chd8*$^{+/-}$ mice compared to controls, as measured by time spent investigating the odour (Fig. 2C). No difference in the investigation of a non-social (banana) odour was observed, implying an increased interest specifically in social cues and otherwise normal capacity for odour discrimination (Fig. 2C).

No evidence of repetitive behaviours was observed by assessing marble burying or self-grooming behaviours (Fig. 2D,E). In fact, mutants showed slightly delayed marble burying behaviour (Fig. 2D). Examination of these animals in the open field arena revealed a marked hypo-activity in *Chd8*$^{+/-}$ mice (Fig. 2F,G). The open field test did not show any evidence of behaviours typically associated with anxiety in mice, i.e. an increased reluctance to enter the inner, most exposed area of an open field arena (Fig. 2H). The hypo-active phenotype was also present in mice in their homecage environment by measuring activity on a running wheel over a one-week period (Fig. 2I). Slightly weaker forelimb grip strength was measured in mutant mice (Fig 2J) but *Chd8*$^{+/-}$ mice showed normal abilities on the revolving rotarod, indicating that the hypo-active phenotype was not due to general motor deficits (Fig. 2K). Finally, no differences in the number of ultrasonic vocalisations (USVs) of pups separated from the nest were recorded, indicating no obvious communication deficits (Fig. 2L).

Chd8 heterozygous pups showed evidence for delayed motor development in the first two weeks after birth. *Chd8*$^{+/-}$ pups took significantly longer than wildtype littermates to develop an effective righting reflex over time (Figure 2M), and correspondingly spent more time engaged in unsuccessful attempts to turn over on their stomachs (Figure 2N). Once they were able to move around the cage, pups showed evidence of hyperactivity (Figure 2O).

In summary, adult *Chd8*$^{+/-}$ mice consistently exhibited a hypo-active phenotype while pups showed evidence for hyperactivity. Chd8$^{+/-}$ mice showed little evidence of typical autism-like behaviours. Rather, a heightened interest in social cues was observed in *Chd8*$^{+/-}$ mice, suggestive of borderline effects on the response of these mice to social cues.

***Chd8* haploinsufficiency causes postnatal brain overgrowth coupled with reduced body weight.**

To characterise the developmental delay observed during behavioural testing and the brain overgrowth phenotype detected by MRI analysis further, postnatal body weight trajectories were established and correlated with brain weights at different developmental stages. A survey of body weight during postnatal development identified significant growth retardation of Chd8$^{+/-}$ pups from postnatal day 4 that culminates in a highly significant statistical difference between the two groups at P35 (15.8%, $p<0.001$, Fig. 3A). Brain weights show a strong correlation with body weight. We therefore correlated brain and body weight in individual animals of Chd8$^{+/-}$ mice at P35 (Fig. 3B). Brain and body weight were positively correlated in both wildtype and heterozygous mice ($r^2=0.25$ and $r^2=0.28$, respectively) and it was evident that *Chd8* mutants with equivalent body weight displayed higher brain weights than their littermate controls (Fig. 3B). Consequently, *Chd8*$^{+/-}$ mice showed a highly significant increase in brain weight normalised to body weight relative to wildtype littermates (Fig. 3C; 20.4% increase, $p<0.001$).

To identify the time when these changes emerge, normalised brain weights were measured at different developmental time points. At P7, normalised brain weights were already significantly larger in *Chd8*$^{+/-}$ pups compared to wildtype littermate controls, with more subtle changes observed at P0, suggesting that the phenotype emerged around this time. Indeed, the same analysis at E16.5 suggested a trend but did not detect any significant differences in *Chd8*$^{+/-}$ embryos (Fig. 3D). Together, these analyses suggested that small differences in differential brain growth over several days during late embryonic and early postnatal development may be responsible for small, progressive increases in brain size. In support of this, we did not detect any significant differences in cortical ventricular zone (VZ) proliferation as measured by phospho-histone H3 immunostaining at E12.5, E16.5 and P0 (Fig. 3E,F).

In summary, our analyses of brain weights were in agreement with the volumetric changes detected by MRI in adult mice and implicated an uncoupling of postnatal brain growth from overall growth as a potential cause of the macrocephalic phenotype observed in patients with *CHD8* mutations. Moreover, the developmental motor delay observed in *Chd8*$^{+/-}$ pups was underpinned by delayed acquisition in body weight in the first few weeks after birth, a phenotype that resolved by 3 months of age, when body weights of *Chd8* heterozygous mice were indistinguishable from wildtype littermate controls (data not shown).

CHD8 controls the expression of ASD-associated genes in early postnatal neocortex

To determine the transcriptional programmes that may underlie the subtle brain overgrowth and abnormal behaviours observed in *Chd8*$^{+/-}$ mice, we performed RNA-seq on dissected neocortical tissue at E12.5, when *Chd8* expression peaks (22), as well as at P5, when many developmental processes with relevance for ASD aetiology (neuronal differentiation, migration and synaptogenesis) are taking place.

Surprisingly, only 5 genes showed significant (FDR<0.0.5) differential expression in *Chd8*$^{+/-}$ embryos at E12.5 (Fig. 4A, Supplementary Table 2). In contrast, 649 genes (FDR<0.05) were differentially expressed in the neocortex at P5, with over two thirds of them downregulated (Fig. 4B, Supplementary Table 3).

Overall, this is in keeping with our findings of postnatal brain overgrowth, where we found little evidence for gross abnormalities in embryonic cortical development.

Comparing all DEGs from the P5 dataset with the SFARI autism gene list identified 57 ASD-associated genes, representing a highly significant enrichment of ASD-associated genes in the DEGs ($p=4.22x10^{-11}$ (OR=2.92), Fisher's exact test for count data, Fig. 4C, Supplementary Table 4). The vast majority of these ASD-associated genes were down-

regulated (95%, Supplementary Table 4), suggesting that some of these expression changes may indeed contribute to relevant phenotypic changes. The overlap was even more robust when limited to high confidence (SFARI category 1&2) ASD candidates ($p=8.1x10^{-5}$ (OR=5.03), Fisher's exact test for count data Fig. 4D), with all of these genes downregulated (Supplementary Table 4).

Amongst the upregulated gene set, the most significant KEGG pathways and biological processes were related to the ribosome and oxidative phosphorylation, whereas the downregulated gene set included categories related to cell adhesion, axonal guidance and calcium signaling pathways (Fig. 4E, Supplementary Fig. 2A, Supplementary tables 5-10). Identification of potential regulatory transcription factors was performed using Enrichr, which found over-representation of Suz12 targets in the down-regulated gene set (Supplementary Fig. 2B). The PRC2 complex, of which Suz12 is a component, leads to transcriptional repression of target genes offering a potential mechanistic explanation for the downregulation of some of the identified genes.

The significant enrichment of cell adhesion and axonal guidance genes in the down-regulated gene setat P5 suggested that long-range connectivity and synaptogenesis might be disrupted in *Chd8* heterozygous neocortices. We hypothesized that these gene expression changes may lead to functional alterations in mature networks.

Chd8$^{+/-}$ mice exhibit over-connectivity in cortical and subcortical networks

To test whether the observed gene expression changes at P5 indeed caused functional anomalies in the adult brain we performed resting state functional MRI (rsfMRI).

This analysis found evidence for over-connectivity between sub-cortical and cortical structures suggestive of aberrant auditory processing. A global analysis for connectivity

properties revealed hotspots for increased connectivity in *Chd8*$^{+/-}$ mice, which included parietal cortex, auditory cortex and hippocampus (Fig. 5A). We next used a seed-based approach to specifically probe regions with altered connectivity to these hotspots. This revealed a reciprocal increase in connectivity between ventral hippocampus and auditory-parietal cortical regions in *Chd8* mutant mice (Fig. 5B), suggestive of aberrant processing or integration of auditory information.

To our knowledge these findings provide the first evidence of apparent hyper-connectivity in the auditory processing pathway in an ASD mouse model.

DISCUSSION

CHD8 is one of the highest confidence autism-associated genes to emerge from recent exome sequencing studies in autism patients (Bernier et al., 2014; Iossifov et al., 2014; Neale et al., 2012; O'Roak et al., 2012; Talkowski et al., 2012). We therefore sought to determine the function of this gene during brain development in vivo. Here, we report structural and functional brain phenotypes in a *Chd8* heterozygous mouse model. These mice further display postnatal growth retardation and distinctive behavioural anomalies that show overlap with symptoms seen in patients but do not include autism-like behaviours.

Gene expression analysis further revealed transcriptional dysregulation of key developmental processes involved in establishing brain connectivity in the early postnatal neocortex. Many of these dysregulated transcripts are themselves ASD-associated genes. Importantly, disruption of these brain wiring pathways results in apparent abnormal functional connectivity in the adult brain. Resting state functional MRI analysis found evidence for over-connectivity in networks that involve the auditory cortex, hippocampus and parietal cortical areas. These findings identify *Chd8* as a gene with important neurodevelopmental functions and provide direct evidence that *CHD8* haploinsufficiency is responsible for a constellation of specific developmental abnormalities.

Chd8$^{+/-}$ mice as a model for human *CHD8* haploinsufficiency syndrome

We report several phenotypes in *Chd8*$^{+/-}$ mice that have been associated with CHD8 haploinsufficiency in humans. This includes hypertelorism and delayed motor development. We also describe postnatal brain overgrowth when correcting for body weight, which may underlie the macrocephaly observed in the majority of patients described in Bernier et al. (2014). Together, these findings indicate that function of CHD8 is largely conserved between

mouse and man, with previous studies suggesting that this also true for non-mammalina species such as zebrafish (10, 17).

Despite the high prevalence of autistic behaviours observed in human *CHD8* haploinsufficiency, *Chd8*$^{+/-}$ mice do not exhibit socio-communicative deficits, repetitive or perseverative behaviours. This is apparently at odds with recent studies of other *Chd8* heterozygous mouse models that reported social deficits (18, 19). However, the results reported in those studies are subtle and accompanied by unusually high levels of anxiety in all test groups (18). Intriguingly, our tests revealed an apparent heightened interest in social cues, indicating that altering the *Chd8* gene dosage during development can impact socially motivated behaviours. A key characteristic of autism is restricted behaviours or interests, which often manifest as hyper- or hypoactivity to sensory input or unusual interest in sensory stimuli, for example excessive smelling or touching of objects (23). One may speculate that the excessive smelling of social cues observed in *Chd8*$^{+/-}$ mice may be related to these abnormal behaviours.

To our knowledge, no other ASD mouse model shows the same behavioural complement we describe for *Chd8*+/- mice. Of note, however, an *Fmr1* knockout mouse shows increased active social interactions, including sniffing, in a social interaction test (24).

Several genes that are de-repressed in the *Fmr1* knockout mouse, are also up-regulated in *CHD8*–deficient human neural stem cells (17), suggesting some molecular genetic similarities between these two mouse models. A *Shank3* mutant mouse model shows a similar hypo-active response to novel environments (25). Intriguingly, the structural brain changes seen in our *Chd8*$^{+/-}$ mouse model, in particular the enlarged frontal and cingulate cortex and hippocampus, are also present in *Shank3* and *Fmr1* mutant mice (26), further suggestive of pathological similarities between these models.

Our data begs the question as to whether the *Chd8*$^{+/-}$ mouse is a good model for understanding the neurobiological basis of autism. These mice clearly recapitulate several characteristic features of humans with *CHD8* mutations, validating this mouse as a model for *CHD8* haploinsufficiency syndrome. However, it does not exhibit social deficits, repetitive behaviours and restricted behaviours, behaviours usually taken as providing "face validity" for autism in rodent models (27). We propose that the robust, abnormal behaviours seen in these mice, in particular in the social domain, point to disruption of fundamental brain circuits and neuronal function that underlie autistic behaviours in humans. In other words, *Chd8* haploinsufficiency may reveal behavioural axes with potential utility for the assay of autism therapeutics, despite their apparent non-similarity to human autism. The identification and further in-depth analysis of these circuits will be an important avenue of future research.

Dysregulation of the cortical transcriptome in *Chd8* heterozygous mice.

Chd8 levels peak at E12, and gradually decline during embryonic development and into postnatal stages (17). Interestingly, our data show that *Chd8* heterozygosity has little effect transcriptionally at E12.5, but by early postnatal stages widespread transcriptional dysregulation is apparent. One possible explanation for this could be that the higher absolute levels of *Chd8* at E12.5 are sufficient to maintain normal gene expression even in the heterozygous state, but as *Chd8* levels fall in late embryonic and early postnatal stages the gene dosage provided by a single functional copy of *Chd8* is no longer sufficient to maintain a normal transcriptomic programme. A second possibility is that *Chd8* heterozygosity influences dysregulation of regulatory genes during early embryogenesis, causing dysregulation of downstream genes, which in turn result in a cascade of differential expression of other genes as development proceeds. In support of this idea, *Chd8* is a known

binding partner of *ß-catenin* and regulator of wnt signalling, a major developmental pathway that plays key roles in specification of cell fate and proliferation (28).

An expanding number of ASD risk genes have roles in axon guidance, synapse development and plasticity (29). Intriguingly, we detected significant enrichment of genes involved in axon guidance and neuron migration in our downregulated gene set; which include the major Slit protein receptors *Robo1* and *Robo2* (Supplementary tables 3 & 6). Slit proteins are critical for establishing several major axonal tracts in the developing forebrain (30). In addition, downregulated genes in P5 heterozygous animals were enriched for cell adhesion molecules, including *L1cam*, which has important roles in neuron migration, neurite outgrowth, modulation of actin cytoarchitecture and axon targeting (31). Taken together, these findings indicate that *Chd8* heterozygosity defines a transcriptional programme characterised by diminished expression of key neurodevelopmental regulators that are predicted to affect a complement of cellular functions essential for the appropriate wiring of the brain.

Increased functional connectivity in sensory networks

RsfMRI revealed altered connectivity in several cortical networks in *Chd8*$^{+/-}$. It is tempting to speculate that altered connectivity is causally linked to some of the disrupted brain wiring pathways uncovered by our RNAseq experiments, but this hypothesis will require further in–depth scrutiny. More importantly, it will be critical to investigate whether these connectivity changes are pertinent to any of the behavioural anomalies in *Chd8* heterozygous mice or autism in general. Intriguingly, we see over-connectivity in networks involving the auditory cortex and ventral hippocampus. Auditory processing deficits have long been described in ASD. They range from a lack of lateralisation to general delay in network maturation (32, 33). The over-connectivity seen in our mouse model could suggests auditory sensory

hypersensitivity. This may also explain the divergent results obtained in different studies concerning social deficits, as a possible environmental stressors might be amplified by sensory hypersensitivity thereby confounding the results of social interaction tests.

Importantly, our data provide the first indication that long-range connectivity is altered in a Chd8$^{+/-}$ mouse model. Interestingly, a recent rsfMRI study involving over 150 male probands with an ASD diagnosis and nearly 200 typically developing individuals described over-connectivity between sensory cortices and subcortical structures as a central feature in ASD (34). It will be very important to determine whether similar abnormalities are detected in patients with *CHD8* haploinsufficiency.

To our knowledge, no other autism mouse model shows the same connectivity changes as we describe here; it will be important to see whether *Shank3* and *Fmr1* mutant mice present with rsfMRI signals similar to *Chd8* mutants.

Taken together, we show that *Chd8*-deficient mice recapitulate craniofacial phenotypes seen in patients and have a unique complement of behavioural anomalies. Moreover, *Chd8*-deficient mice display dysregulation of cortical gene expression networks that are intricately linked to brain wiring, and apparent hyper-connectivity of sensory networks in the brain.

METHODS

Chd8 gene targeting

A 14.84 kb genomic DNA fragment was subcloned from C57BL/6 BAC clone (RP23: 318M20) into pSP72 (Promega). This fragment encompassed a long homology arm (LA) of 9.45kb 5' and a short homology arm (SA) of 4.4kb 3' of the site to be targeted. The targeting construct was generated by inserting a loxP/FRT-PGK-gb2-Neo cassette 214bp 3' of exon 3 (ingenious targeting laboratory (iTL), Ronkonkoma, NY, USA). An additional single loxP site containing a BclI restriction site for Southern blot screening was inserted 5' of exon 3. The final targeting construct of 18.8 kb was linearised by NotI digestion and electroporated into C57BL/6J ES cells. G418-resistent clones were selected, screened by PCR and Southern blot for successful homologous recombination. Five clones with successful recombination were identified (Figure S1) and two clones (124 and 254) were injected into Balb/c blastocysts (iTL). Resulting chimaeras were bred either with C57BL/6J mice to maintain the *Chd8*$^{neo/+}$ line, or with Flpe delete mice on a C57BL/6J background to excise the neo cassette and produce *Chd8*$^{flox/+}$ mice (Figure 1).

Mice

Chd8$^{flox/+}$ mice were bred with *β-actinCre* mice (35) to generate a *Chd8* null (*Chd8*$^{-}$*)* allele. *β–actinCre;Chd8*$^{+/-}$ mice were crossed with C57BL/6J mice to remove the Cre transgene and establish a *Chd8*$^{+/-}$ line. Experimental mice were produced by *Chd8*$^{+/-}$ x C57BL/6J crosses, taking care to equalise paternal or maternal inheritance of the *Chd8* null allele, especially for behavioural experiments.

For genotyping, genomic DNA was routinely extracted from ear or tail samples (or yolk sac for E12.5 embryos) using Proteinase K digestion or the HotSHOT method (36). Genotyping reactions were then performed for the presence of *Chd8* wildtype and null alleles using the following primer pair: FW: CCC ACA TCA AGT GGC TGT AA, Rev: GGT AGG GAA GCA GTG TCC AG. Thermal cycles for were as follows: 94°C, 5 minutes; 35X (94°C, 30sec; 58°C, 30sec; 72°C, 30sec); 72°C, 5 minutes. This yielded a PCR product of 395bp for the null allele and 1.1kb for the wildtype allele.

Western Blot

Telencephalic vesicles were dissected from E12.5 embryos and whole cell protein prepared by lysing in 8M urea, 1% CHAPS, 50mM Tris (pH 7.9) lysis buffer containing protease

inhibitors (PMSF, Pepstatin A, Leupeptin, Aprotinin; Roche) and a phosphatase inhibitor cocktail (Sigma). Lysates were rotated at 4°C for 3 mins followed by DNA removal by centrifugation. Supernatant was transferred to fresh tube and stored at -80°C. Protein loading samples were made by diluting samples in Laemmli buffer containing 10% β-mercaptoethanol, followed by boiling at 95°C for 5 minutes.

Samples were loaded (10µg total protein per lane) onto a Mini-PROTEAN pre-cast gel (Bio-Rad) and resolved using gel electrophoresis. Protein was transferred to a nitrocellulose membrane (Bio-Rad) which was then blocked in 5% non-fat milk powder (Bio-Rad) and 1% bovine serum albumin (BSA, Sigma) in TBS with 0.1% Tween-20 (TBST) for one hour at room temperature, followed by incubation with anti-CHD8 primary antibody (rabbit anti-Chd8 N-terminal, Bethyl Laboratories, 1:5000) in 3% non-fat milk powder and 1% BSA in TBST overnight at 4°C. After washing, membrane was incubated with HRP-conjugated secondary antibody (Millipore) for one hour at room temperature. HRP was detected with Clarity ECL reagent (Bio-Rad) and the membrane imaged using a Bio-Rad ChemiDoc system. The membrane was then washed in TBST and incubated overnight at 4°C in 0.05% sodium azide in PBS, before washing and incubation with anti-GAPDH primary antibody (rabbit anti-GAPDH, Abcam, 1:40000) overnight at 4°C. Membrane was probed with HRP-conjugate and imaged as before. Relative protein quantity was calculated using Bio-Rad ImageLab software.

X-ray Computed tomography

Fixed heads from adult (26 - 27 days old) *Chd8*$^{+/-}$ and *Chd8*$^{+/+}$ mice (n=7 of each from two different litters) were scanned using a GE Locus SP microCT scanner. The specimens were immobilised using cotton gauze and scanned to produce 28µm voxel size volumes, using a X-ray tube voltage of 80kVp and a tube current of 80uA. An aluminium filter (0.05mm) was used to adjust the energy distribution of the X-ray source. Reconstructions of computer tomography scans, images and measurements were done in MicroView 2.5.0 software from Parallax Innovations. Each 3D landmark point was recorded, twice for each sample, using the 3D point recording built-in tool within the same software, with the operator blind to the genotypes. The distances between the landmarks were normalised for each sample to the average of the wild-type littermates. Graphics of the plotted data and statistical analysis were performed using GraphPad Prism version 6.0h for Mac OS X, GraphPad Software, La Jolla California USA, www.graphpad.com. Unpaired student t-tests were applied to analyse the variation between the two groups, for every distance between 2 specific 3D landmark points.

Three-dimensional coordinate locations of a total of 22 biological relevant cranial landmarks were chosen based on the landmark list for adult mouse skull proposed by the Richtsmeier lab (http://getahead.psu.edu/landmarks_new.html) (37).

3D LANDMARK POINTS LIST:

1.- Nasale: intersection of nasal bones at midline, rostral point

2.- Nasion: intersection of nasal bones at midline, caudal point

3.- Bregma: intersection of frontal bones and parietal bones at midline

4.- Lambda: intersection of parietal bones with anterior aspect of interparietal bone at midline

5.- Intersection of interparietal bones with squamous portion of occipital bone at midline

6.- Anterior-most portion at intersection of premaxillae and nasal bones, left side

7.- Anterior-most portion at intersection of premaxillae and nasal bones, right side

8.- Anterior notch on frontal process lateral to infraorbital fissure, left side

9.- Anterior notch on frontal process lateral to infraorbital fissure, right side

10.- Frontal-squasmosal intersection at temporal crest, left side

11.- Frontal-squasmosal intersection at temporal crest, right side

12.- Joining of squasmosal body to zygomatic process of squasmosal, left side

13.- Joining of squasmosal body to zygomatic process of squasmosal, right side

14.- Intersection of parietal, temporal and interparietal bones, left side

15.- Intersection of parietal, temporal and interparietal bones, right side

16.- Most anterior point of the anterior palatine foramen, left side

17.- Most anterior point of the anterior palatine foramen, right side

18.- Most posterior point of the anterior palatine foramen, left side

19.- Most posterior point of the anterior palatine foramen, right side

20.- Posterior nasal spine, most posterior projection of the posterior nasal spine (palatine bone)

21.- Basion: midsaggital point on the anterior margin of the foramen magnum

22.- Opisthion: midsaggital point on the posterior margin of the foramen magnum

Tissue Collection and Processing

Pups were weighed and then sacrificed, while embryos were collected by dissection in ice-cold PBS, excess PBS drained and whole embryos weighed. Brains were then dissected from the skull in ice-cold PBS and cut below the brain stem. Brains were then immediately drained on paper towels using a slotted spoon and wet weights determined using a fine scale. Brains

were returned to PBS and wholemount pictures taken on a Nikon SMZ1500 stereo-microscope equipped with a Nikon DS-Fi1 camera head, before post-fixation in 4% PFA at 4°C for 24h. After fixing, embryos were dehydrated and paraffin embedded. Paraffin blocks were then cut into 10µm thick coronal sections and mounted such that each slide contained three adjacent sections.

Immunohistochemistry

Coronal brain sections were re-hydrated using standard protocols. Antigen retrieval was conducted by heating slides in 10mM Sodium Citrate solution (pH6) for 20mins and cooled on ice. Endogenous peroxidases were blocked by incubating in 3% H_2O_2 and 10% MeOH in PBS for 15mins. Sections were then washed in 0.2% Triton X-100 (Sigma-Aldrich) in PBS (PBT2) for 5 mins and blocked using 10% heat-inactivated normal goat serum (GS) and 2% gelatin in PBT2 for 1 hour. Sections were incubated in 5% GS in PBT2 containing primary antibody overnight at 4°C. The following antibodies were used: rabbit anti-phosphohistone 3B (Cell Signaling, 1/100). After incubation with primary antibody, sections were incubated in biotinylated anti-rabbit immunoglobulin secondary antibody (Dako, 1/200) in 5% GS in PBT2. Samples were washed in PBS and incubated with Avidin/biotin complex (ABC, Vector) in PBS for 1 hour. Sections were developed using 0.025% DAB and 0.03% H_2O_2 in PBS for 10mins before washing in running water and counterstaining using Ehrlich's Hemotoxylin solution. Slides were mounted onto coverslips using DPX (Sigma-Aldrich). Images were acquired on a Nikon 80i microscope equipped with a Nikon 5M pixel Nikon DS digital cameras. Images were processed using Adobe Photoshop and Illustrator.

Quantitative Analysis

Proliferation was quantified by counting phosphohistone 3B-positive cells lining the ventricular surface of the dorsal cortex and normalised to the length of ventricular surface. These were quantified on both sides of the brain in three consecutive sections and averaged to calculate the number of phosphohistone 3B-positive cells per µm of ventricular surface in the dorsal cortex. All data were analysed using GraphPad Prism 6 and significance calculated using student's t-test.

Behavioural assessments

Mice for behavioural testing were housed in standard cages measuring 32×16×14cm with sawdust (Litaspen premium, Datesand Ltd, Manchester), a cardboard shelter and additional

bedding material (Sizzlenest, Datesand Ltd, Manchester) with *ad libitum* access to water and food (Rat and Mouse No. 1 and 3 Maintenance Diet for test and breeding mice respectively, Special Diet Services, Essex, UK). The housing and test rooms were maintained at constant room temperature (21°C) and humidity (45%) and kept under a regular light/dark schedule with lights on from 07:30 to 19:30 hours (light = 270 lux).

Different batches of *Chd8*$^{+/-}$ mice were used for (i) recording pup USVs and spontaneous movements, and (ii) juvenile and adult behaviours. For the first batch of mice, paw tattoos were administered, immediately after testing on P2, to allow for identification of pups. All batches of mice were ear notched for permanent identification at P14 and housed in same-sex groups of 2-3 after weaning (P21). For juvenile-adult behaviours in *Chd8*$^{+/-}$ mice, tests were carried out in the following order: juvenile social investigation, rotarod, open field, self-grooming, marble burying, adult social investigation, 3 chamber social approach, light/dark test, and olfactory habituation/dishabituation.

One week before performing the rotarod test, mice were singly-housed to avoid any potential confounds from social- and aggressive behaviour hierarchies, which could influence the controlled assessment of social behaviours (38). Sawdust was changed every other week but never on the day before, or the day of, testing and the enrichment (nesting material and house) was changed less regularly to minimize the disruption to the animals. For all social tests, conspecific mice were housed in a separate room to the test mice to ensure the conspecifics were unfamiliar to the test mice. Test mice were never exposed to the same conspecific during testing to ensure novelty.

Behavioural experiments were conducted between 08:30 and 18:30 in sound-proofed rooms under standard room lighting unless stated otherwise. Behaviours were recorded using a camera positioned above the test arenas and movement of each mouse tracked using EthoVision (Noldus Information Technologies bv, Wageningen, The Netherlands), or scored manually using NOLDUS OBSERVER software V 10XT (Noldus Information Technology, Wageningen, NL, USA). After each individual trial of a specific test, boli and urine were removed from the test arena which was cleaned with 1% Anistel® solution (high level surface disinfectant, Trisel Solution Ltd, Cambridgeshire, UK) to remove any odors. Experimenters were blind to the genotype of the animals both during the testing and subsequent scoring of the recorded behaviours.

Ultrasonic vocalisations (USV) in response to maternal & nest separation: Ultrasonic vocalisations (USVs) were recorded in pups across 3min sessions in response to social separation from the mother and siblings at P2, 4, 6, 8 and 12. An Ultrasound Microphone (Avisoft UltraSoundGate condenser microphone capsule CM16, Avisoft Bioacoustics, Berlin, Germany), sensitive to frequencies of 10–180 kHz, was placed through a hole in the middle of the cover of the sound-attenuating box, about 20 cm above the pup in its glasses container. Vocalisations were recorded using Avisoft Recorder software (Version 3.2). For acoustical analysis, recordings were transferred to Avisoft SASLab Pro (Version 4.40) and a fast Fourier transformation (FFT) was conducted. Spectrograms were generated at a frequency resolution of 488 Hz and a time resolution of 1 ms. Number of calls for each day of testing has been analysed to define the ontogenetic profile of emission in control and conditional knockout pups, as described previously (39). Simultaneously, spontaneous motor behaviours were recorded, as described (40).

Grip Strength: To assess the neuromuscular ability of the animals, fore- and hindlimb grip strength was measured using a Linton Grip Strength Meter (MJS Technology Ltd, Stevenage UK). Fore- and hindlimb grip strength was measured 3 times and the mean grip strength of the 3 trials reported (41).

Rotarod: Motor coordination and learning were assessed on a rotating rod (Ugo Basile, Milan, Italy) as described (42), with the exception that the maximum speed was set to 30rpm for *Chd8*$^{+/-}$ mice. The latency to fall for any particular day was calculated as the mean of 2 trials.

Open field: Mice were placed facing the wall of a circular open field arena (40 cm diameter) and allowed to freely explore for 10 min. An area of equal distance from the periphery (20 cm diameter), defined as the 'central zone' which is assumed to be the more anxiolytic part of the arena, was virtually drawn in Ethovision.

Light/dark box: a custom-built box of grey acrylic was used with dimensions (44 x 21 x 21 cm). The box was divided into two chambers by a sheet of grey acrylic (21 x 50 cm); a smaller dark chamber (20 lux) that occupied roughly 1/3 of the total box, and a larger light chamber (80-110 lux) that was lit from above with a bright white light. A small doorway

within the partition, 5 x 7 cm, allowed the mice to move between chambers freely. Mice were placed in the dark compartment at the start of the 5-min trial. The latency (s) to enter the light chamber, time (s) spent in each chamber, and the numbers of light-dark transitions were measured. The mean velocity (cm/s) and total distance travelled (cm) in the dark and light compartments were extracted from the tracking software. Entry to either compartment was defined as when all four paws of the mouse had entered in one compartment.

Self-grooming: This test was carried out as described (43). The animals were placed in an empty standard housing cage (Tecniplast cage, 32cm x 16cm x 14cm) and given 10 minutes to habituate in a dimly lit test room (< 10 lux). The cumulative time spent self-grooming in the following 10 minutes was recorded by an experimenter blind to the genotype of the mouse. Locomotor activity (distance travelled, cm; velocity, cm/s) of the mice was tracked using the Ethovision software.

Marble burying: Repetitive digging behaviour to bury marbles was measured, as described by Deacon, 2006. Repetitive digging behaviour to bury marbles was measured in a dimly lit test room (< 10 lux). Twelve blue glass marbles were arranged in a symmetrical 4×3cm grid on top of 5 cm deep sawdust (Litaspen premium, Datesand Ltd, Manchester) in a clean, standard housing cage (32×16×14cm). Each mouse was given 30min to freely explore the cage. Eight mice were tested simultaneously and the number of marbles buried at 2.5, 5, 7.5, 10, 20 and 30 min intervals were counted by the experimenter.

Juvenile social investigation: Social investigation of age- and sex-matched C57BL/6J conspecifics was assessed in juvenile test mice (P21) as described (44), with the exception that mice were not habituated to the test room and behaviours only recorded for 15 minutes. Mice were singly housed on P21, in a clean, standard housing cage (32×16×14cm) with sawdust (Litaspen premium, Datesand Ltd, Manchester) but no other enrichment and with ad libitum access to food and water. After 1h, test mice were placed into a new standard housing cage containing sawdust and a novel, juvenile (3 weeks old) sex-matched conspecific C57BL/6J mouse introduced to the test cage. The test room was dimly lit (10 lux). Mice were allowed to interact for 15 min and the behaviour was recorded. The following behaviours (frequency and duration in s) initiated by the test mouse were scored: anogenital sniffing (direct contact with the anogenital area), body sniffing (sniffing or snout contact with the flank area), head sniffing (sniffing or snout contact with the head/neck/mouth area). No

observations of mounting, fighting, tail rattling, and wrestling behaviours were observed. Scoring was conducted by an experimenter blind to the genotype of the mouse.

Adult social investigation: Social investigation and USV emission of test mice in response to C57BL/6J sex-matched conspecifics were assessed in adulthood. Test mice were placed into a new standard housing cage containing sawdust and a novel, sex-matched conspecific C57BL/6J mouse introduced to the test cage. The test room was dimly lit (10 lux). Mice were allowed to interact for 3 minutes and the behaviour was recorded. Social investigation (sniffing around the head, body and anogenital regions) initiated by the test mouse subsequently was scored from the recordings by an experimenter blind to the genotype of the mouse. No observations of mounting, fighting, tail rattling, and wrestling behaviours were observed. Furthermore, social investigation and USV emission of male test mice in response to C57BL/6J females in estrous or pro-estrous were also assessed in adulthood as described (45).

3 Chamber social approach: This task was essentially carried out as described (46), with 2 alterations: (1) the chamber was not automated and instead Ethovision was used to track the activity of the test mouse and (2) a novel object (tally counter, Appleton Woods GC101) was placed under the cup in trial 2. The mice were allowed to freely explore the three-chamber apparatus over two 10 min trials. During trial 1, the apparatus was empty and the locomotor activity (distance travelled, cm; velocity, cm/s) of, and time (s) spent in each chamber by, the mouse was tracked using Ethovision. In trial 2, one wire cup containing the inanimate object was placed upside down in one of the side chambers (novel object stimulus) and a novel age and sex-matched conspecific mouse was placed under another wire cup in the other side chamber (novel mouse stimulus), leaving the middle chamber empty. The location of the novel mouse across trials was counterbalanced to minimize any potential confound due to a preference for chamber location.

Olfactory habituation/dishabituation test: This task was essentially carried out as described (47). Animals were tested in their home cage, with all the enrichment removed and a fresh cage lid provided just before the trial commenced to minimize the amount of interfering odors. (The cage of each mouse was cleaned 3 days prior to testing). Following a 10 min habituation, the mouse was exposed to three odors in turn: water (control/no odor; 50µl), banana essence (non-social; 50µl; Uncle Roy's, Moffat, UK) and urine collected from novel,

sex-matched conspecific mice (social, 25µl), each presented on a cotton-tipped wooden applicator 3 times over 2 minutes. Total time (s) spent by the mouse sniffing the cotton buds during each trial was recorded.

General activity measurements

General activity was measured using a running wheel paradigm. Mice were housed individually under a 12h:12h light-dark cycle (lights on at 8am; lights off at 8pm) in a light-, air-, temperature-controlled ventilated cabinet (Arrowmight, Hereford, UK). Running-wheel cages were equipped with an infrared sensor (Bilaney consultant Ltd, Sevenoaks, UK) connected to a computer. Data were collected in 1-min bins using Clocklab software (Actimetrics, Inc, Wilmette, IL, USA). Mice were continuously monitored undisturbed from the day they were placed in the running wheel cages and their general activity during the light versus dark phase were compared over the first 7 days using a three-ways (sex X genotype X activity) analysis of variance (ANOVA). Since male and female mice did not show any statistical significant sex difference, data were pooled.

Statistical analysis: All statistical analyses were conducted using SPSS (Statistics 22 (IBM, Version Armonk, USA). Data were analyzed using either a between-subjects ANOVA or a 2-way repeated measures ANOVA, as appropriate. The between-factors were always sex and genotype, and within-factors either were time (olfactory habituation/dishabituation) or chamber (three-chamber social approach task). When the appropriate ANOVA showed a significant effect for a particular task, a student's t-test was used to verify the group (open field activity, 3 chamber, marble burying) or the trial (olfactory habituation/dishabituation) that was responsible for effect. Student's t-tests were used as post-hoc analyses, as there were only 2 groups for comparison.

Structural MRI

After completion of adult behavioural tests, mice were terminally anesthetized and intracardially perfused with 30mL of 0.1M PBS containing 10U/mL heparin (Sigma) and 2mM ProHance (a Gadolinium contrast agent) followed by 30mL of 4% paraformaldehyde (PFA) containing 2mM ProHance (48). Perfusions were performed at a rate of approximately 60mL/hr. After perfusion, mice were decapitated. The brain and remaining skull structures were incubated in 4% PFA + 2mM ProHance overnight at 4°C then transferred to 0.1M PBS containing 2mM ProHance and 0.02% sodium azide for at least 7 days prior to MRI

scanning. A multi-channel 7.0 Tesla MRI scanner (Varian Inc., Palo Alto, CA) was used to image the brains within skulls. Sixteen custom-built solenoid coils were used to image the brains in parallel (49). Parameters used in the anatomical MRI scans: T2- weighted 3D fast spin-echo sequence, with a cylindrical acqusition of k-space, and with a TR of 350 ms, and TEs of 12 ms per echo for 6 echoes, two averages, field-of-view of 20 x 20 x 25 mm^3 and matrix size = 504 x 504 x 630 giving an image with 0.040 mm isotropic voxels (50). The current scan time required for this sequence is ~14 hours. To visualise and compare any changes in the mouse brains the images were linearly (6 parameter followed by a 12 parameter) and non-linearly registered towards a pre-existing atlas (51), and then iteratively linearly and non-linearly aligned to each other to create a population atlas representing the average anatomy of the study sample. The result of the registration is to have all scans deformed into alignment with each other in an unbiased fashion. This allows for the analysis of the deformations needed to take each individual mouse's anatomy into this final atlas space, the goal being to model how the deformation fields relate to genotype (52, 53). The jacobian determinants of the deformation fields were then calculated as measures of volume at each voxel. Significant volume changes were then calculated in two ways, 1) on a region basis, and 2) voxelwise. Regional volumes are calculated by warping a pre-existing classified MRI atlas onto the population atlas. This atlas encompasses 159 different structures including, but not limited to, the cortical lobes, large white matter structures (i.e. corpus callosum), ventricles, cerebellum, brain stem, and olfactory bulbs (51, 54, 55). Significant differences can then be determined between groups for the 159 different regions in the brain. Voxelwise comparisons were made between mutants and littermate controls. Voxelwise comparisons were then made between mutants and wildtypes, and multiple comparisons in this study were controlled for using the False Discovery Rate (56).

RNA Extraction and qRT-PCR analysis.

To extract RNA, dissected cortices were lysed in 600µl Trizol (Life Technologies). RNA was then purified and DNase treated using the Direct-zol RNA MiniPrep kit (Zymo Research) according to the manufacturer's instructions. For qRT-PCR, cDNA was synthesized using 50ng RNA from 4 biological replicates per condition with the Precision nanoScript 2 Reverse Transcription Kit (PrimerDesign Ltd.) according to the manufacturer's recommendations. qRT-PCRs were performed on a Stratagene Mx3000p (Agilent Technologies) using PrecisionPlus-MX 2x qPCR Mastermix with SYBR green (PrimerDesign Ltd.) and primers against *Chd8* (FW: CAG AGG AGG AGG GTG AAA AGA AAC, Rev: GAG TTG TCA

GAC GAT GTG TTA CGC). *Canx* and *Sdha* (E12.5) and *Gapdh* and *Eifa* (P5) were used as endogenous control genes as determined by prior geNorm (Primerdesign, UK) analysis for the respective sample sets, and relative expression levels were calculated using the $2^{-\Delta\Delta C_T}$ method.

RNA Sequencing

For RNA-sequencing mRNA was isolated from micro-dissected cortices at E12.5 (both hemispheres) and P5 (one hemisphere) and reverse transcribed into cDNA (n=3 per experimental group). cDNA was end-repaired, adaptor-ligated and A-tailed. Paired-end sequencing was performed on the Illumina HiSeq 4000 platform. Quality of the raw sequencing data was checked using FastQC version 0.11.2 and trimming of adaptor sequences was performed using Trim Galore! version 0.4.1 (Krueger 2012; Andrews 2010). Reads were aligned to the mouse genome (GRCm38.p4) using Tophat version 2.1.0 and aligned reads were counted using FeatureCounts version 1.5.0 (Liao et al. 2014; Kim et al. 2013). Differential expression testing was performed using DESeq2 version 1.10.1, as previously described (Love et al. 2014). Gene ontology analysis and functional classification was performed using DAVID with all detected DEGs below a 0.05 FDR (Huang et al. 2009). Putative regulatory transcription factors were determined using Enrichr using the "ENCODE and ChEA Consensus TFs from ChIP-X" database with all DEGs below a 0.05 FDR (Chen et al. 2013). For heatmaps, data were normalised using the trimmed mean of M-values (TMM), mean centre scaled, clustered based on euclidean distance, and plotted with the heatmap.2 function from the R package gplots version 3.0.1. The R package ggplot2 version 2.1.0 was used to generate volcano plots and DESeq2 normalised read count plots for individual genes. The list of ASD associated genes used for overlap with P5 DEGs was obtained from the SFARI Human Gene database (https://gene.sfari.org/autdb/HG_Home.do). RNA-seq data have been deposited into GEO, accession number GSE81103.

Resting-State fMRI

rsfMRI experiments were performed on 15-18 week old mice (n = 23 *Chd8*$^{+/+}$; n = 19 *Chd8*$^{+/-}$). Animals were prepared for imaging as previously described (Ferrari et al. 2012; Sforazzini et al. 2016). Briefly, mice were anaesthetised using isoflurane (5% induction), intubated and artificially ventilated (2% maintenance). Blood pressure was monitored continuously by cannulating the left femoral artery, also allowing for terminal arterial blood

sampling. Administration of isoflurane was ceased after surgery and substituted with halothane (0.75%). 45 mins after isoflurane cessation functional data acquisition commenced. Throughout each imaging session mean arterial blood pressure was recorded continuously.. To evaluate potential genotype differences in anaesthesia sensitivity, Student's 2-sample t-tests were used to compare mean arterial blood pressure and amplitude of cortical BOLD signal fluctuations between genotypes. These independent measures have previously been demonstrated to correlate linearly with depth of anaesthesia (Steff et al. 2003; Liu et al. 2011; Zhan et al. 2014).

In vivo images were obtained using a 7.0 T MRI scanner (Bruker Biospin, Milan), as previously described (Liska et al. 2016). Signal transmission and reception were achieved using a 72mm birdcage transmit coil and a 4-channel solenoid coil. For each session, high resolution anatomical images were acquired using a fast spin echo sequence based on the following parameters: repetition time (TR)/echo time (TE) 5500/60ms, matrix 192 x 192, field of view 2 x 2cm^3, 24 coronal slices, and slice thickness 0.50mm. Co-centred BOLD rsfMRI time series were acquired using an echo planar imaging (EPI) sequence with the following parameters: TR/TE 1200/15ms, flip angle 30°, matrix 100 x 100, field of views 2 x 2cm^2, 24 coronal slices, slice thickness 0.50mm, 500 volumes and 10min total acquisition time. MRI raw data, templates and code employed to generate functional maps are available to readers by contacting AG.

Functional Connectivity Analyses

To allow for T_1 equilibration effects, the first 20 volumes of rsfMRI data were removed. The time series were then despiked, corrected for motion and spatially normalised to an in-house mouse brain template (Sforazzini et al. 2014). Normalised data had a spatial resolution of 0.1042 x 0.1042 x 0.5mm^3 (192 x 192 x 24 matrix). Mean ventricular signal (averaged rsfMRI time course within a reference ventricular mask) and head motion traces were regressed out of each time series. No genotype-dependent differences were observed in ventricular volume, as measured by the dimensions of individual ventricular masks. All rsfMRI time series were then spatially smoothed (full width at half maximum of 0.6mm) and band-pass filtered using a frequency window of 0.01-0.1Hz.

To identify brain regions displaying genotype-dependent differences in functional connectivity in an unbiased manner, we calculated global maps for all subjects, as described previously (Liska et al. 2017).

A previously described seed-based approach was then used to examine between-group differences in the intensity and scope of long-range rsfMRI correlation networks (Sforazzini et al. 2014).

ACKNOWLEDGEMENTS

This work was supported by research grants from the Medical Research Council (MR/K022377/1, MAB and CF), Simons Foundation (SFARI #344763, MAB; SFARI #400101, AG), Ontario Brain Institute's POND programme (JPL), and BBSRC (BB/K008668/1, PFW). SH and RE were supported by the King's Bioscience Institute and the Guy's and St Thomas' Charity Prize PhD Programme in Biomedical and Translational Science. We acknowledge Alex Donovan for technical assistance and Chris Healy for μCT scans. We acknowledge the High-Throughput Genomics Group at the Wellcome Trust Centre for Human Genetics (funded by Wellcome Trust grant reference 090532/Z/09/Z) for the generation of the RNA sequencing data and Drs. Brian Nieman and Leigh Spencer Noakes for their MRI sequences.

REFERENCES

1. APA. Diagnostic and statistical manual of mental disorders. 5th ed. Arlington, VA: American Psychiatric Publishing; 2013.
2. Neale BM, Kou Y, Liu L, Ma'ayan A, Samocha KE, Sabo A, et al. Patterns and rates of exonic de novo mutations in autism spectrum disorders. Nature. 2012;485(7397):242-5.
3. O'Roak BJ, Stessman HA, Boyle EA, Witherspoon KT, Martin B, Lee C, et al. Recurrent de novo mutations implicate novel genes underlying simplex autism risk. Nature communications. 2014;5:5595.
4. O'Roak BJ, Vives L, Girirajan S, Karakoc E, Krumm N, Coe BP, et al. Sporadic autism exomes reveal a highly interconnected protein network of de novo mutations. Nature. 2012;485(7397):246-50.
5. Talkowski ME, Rosenfeld JA, Blumenthal I, Pillalamarri V, Chiang C, Heilbut A, et al. Sequencing chromosomal abnormalities reveals neurodevelopmental loci that confer risk across diagnostic boundaries. Cell. 2012;149(3):525-37.
6. Iossifov I, O'Roak BJ, Sanders SJ, Ronemus M, Krumm N, Levy D, et al. The contribution of de novo coding mutations to autism spectrum disorder. Nature. 2014;515(7526):216-21.
7. Krumm N, O'Roak BJ, Shendure J, Eichler EE. A de novo convergence of autism genetics and molecular neuroscience. Trends in neurosciences. 2014;37(2):95-105.
8. Di Martino A, Yan CG, Li Q, Denio E, Castellanos FX, Alaerts K, et al. The autism brain imaging data exchange: towards a large-scale evaluation of the intrinsic brain architecture in autism. Molecular psychiatry. 2014;19(6):659-67.
9. Liska A, Bertero A, Gomolka R, Sabbioni M, Galbusera A, Barsotti N, et al. Homozygous Loss of Autism-Risk Gene CNTNAP2 Results in Reduced Local and Long-Range Prefrontal Functional Connectivity. Cerebral cortex. 2017:1-13.
10. Bernier R, Golzio C, Xiong B, Stessman HA, Coe BP, Penn O, et al. Disruptive CHD8 mutations define a subtype of autism early in development. Cell. 2014;158(2):263-76.
11. Merner N, Forgeot d'Arc B, Bell SC, Maussion G, Peng H, Gauthier J, et al. A de novo frameshift mutation in chromodomain helicase DNA-binding domain 8 (CHD8): A case report and literature review. Am J Med Genet A. 2016.
12. Stolerman ES, Smith B, Chaubey A, Jones JR. CHD8 intragenic deletion associated with autism spectrum disorder. Eur J Med Genet. 2016;59(4):189-94.
13. Stessman HA, Xiong B, Coe BP, Wang T, Hoekzema K, Fenckova M, et al. Targeted sequencing identifies 91 neurodevelopmental-disorder risk genes with autism and developmental-disability biases. Nature genetics. 2017;49(4):515-26.
14. Yuan CC, Zhao X, Florens L, Swanson SK, Washburn MP, Hernandez N. CHD8 associates with human Staf and contributes to efficient U6 RNA polymerase III transcription. Mol Cell Biol. 2007;27(24):8729-38.
15. Thompson BA, Tremblay V, Lin G, Bochar DA. CHD8 is an ATP-dependent chromatin remodeling factor that regulates beta-catenin target genes. Mol Cell Biol. 2008;28(12):3894-904.
16. Cotney J, Muhle RA, Sanders SJ, Liu L, Willsey AJ, Niu W, et al. The autism-associated chromatin modifier CHD8 regulates other autism risk genes during human neurodevelopment. Nature communications. 2015;6:6404.
17. Sugathan A, Biagioli M, Golzio C, Erdin S, Blumenthal I, Manavalan P, et al. CHD8 regulates neurodevelopmental pathways associated with autism spectrum disorder in neural progenitors. Proc Natl Acad Sci U S A. 2014;111(42):E4468-77.
18. Katayama Y, Nishiyama M, Shoji H, Ohkawa Y, Kawamura A, Sato T, et al. CHD8 haploinsufficiency results in autistic-like phenotypes in mice. Nature. 2016;537(7622):675-9.

19. Platt RJ, Zhou Y, Slaymaker IM, Shetty AS, Weisbach NR, Kim JA, et al. Chd8 Mutation Leads to Autistic-like Behaviors and Impaired Striatal Circuits. Cell reports. 2017;19(2):335-50.
20. Barnard RA, Pomaville MB, O'Roak BJ. Mutations and Modeling of the Chromatin Remodeler CHD8 Define an Emerging Autism Etiology. Front Neurosci. 2015;9:477.
21. Ecker C. The neuroanatomy of autism spectrum disorder: An overview of structural neuroimaging findings and their translatability to the clinical setting. Autism. 2016.
22. Durak O, Gao F, Kaeser-Woo YJ, Rueda R, Martorell AJ, Nott A, et al. Chd8 mediates cortical neurogenesis via transcriptional regulation of cell cycle and Wnt signaling. Nat Neurosci. 2016.
23. Constantino JN, Charman T. Diagnosis of autism spectrum disorder: reconciling the syndrome, its diverse origins, and variation in expression. The Lancet Neurology. 2016;15(3):279-91.
24. Spencer CM, Alekseyenko O, Serysheva E, Yuva-Paylor LA, Paylor R. Altered anxiety-related and social behaviors in the Fmr1 knockout mouse model of fragile X syndrome. Genes, brain, and behavior. 2005;4(7):420-30.
25. Speed HE, Kouser M, Xuan Z, Reimers JM, Ochoa CF, Gupta N, et al. Autism-Associated Insertion Mutation (InsG) of Shank3 Exon 21 Causes Impaired Synaptic Transmission and Behavioral Deficits. The Journal of neuroscience : the official journal of the Society for Neuroscience. 2015;35(26):9648-65.
26. Ellegood J, Anagnostou E, Babineau BA, Crawley JN, Lin L, Genestine M, et al. Clustering autism: using neuroanatomical differences in 26 mouse models to gain insight into the heterogeneity. Molecular psychiatry. 2015;20(1):118-25.
27. Silverman JL, Yang M, Lord C, Crawley JN. Behavioural phenotyping assays for mouse models of autism. Nature reviews Neuroscience. 2010;11(7):490-502.
28. Nishiyama M, Skoultchi AI, Nakayama KI. Histone H1 recruitment by CHD8 is essential for suppression of the Wnt-beta-catenin signaling pathway. Molecular and cellular biology. 2012;32(2):501-12.
29. Bourgeron T. From the genetic architecture to synaptic plasticity in autism spectrum disorder. Nature reviews Neuroscience. 2015;16(9):551-63.
30. Bagri A, Marin O, Plump AS, Mak J, Pleasure SJ, Rubenstein JL, et al. Slit proteins prevent midline crossing and determine the dorsoventral position of major axonal pathways in the mammalian forebrain. Neuron. 2002;33(2):233-48.
31. Maness PF, Schachner M. Neural recognition molecules of the immunoglobulin superfamily: signaling transducers of axon guidance and neuronal migration. Nature neuroscience. 2007;10(1):19-26.
32. Bruneau N, Dourneau MC, Garreau B, Pourcelot L, Lelord G. Blood flow response to auditory stimulations in normal, mentally retarded, and autistic children: a preliminary transcranial Doppler ultrasonographic study of the middle cerebral arteries. Biological psychiatry. 1992;32(8):691-9.
33. Edgar JC, Fisk Iv CL, Berman JI, Chudnovskaya D, Liu S, Pandey J, et al. Auditory encoding abnormalities in children with autism spectrum disorder suggest delayed development of auditory cortex. Molecular autism. 2015;6:69.
34. Cerliani L, Mennes M, Thomas RM, Di Martino A, Thioux M, Keysers C. Increased Functional Connectivity Between Subcortical and Cortical Resting-State Networks in Autism Spectrum Disorder. JAMA psychiatry. 2015;72(8):767-77.
35. Lewandoski M, Martin GR. Cre-mediated chromosome loss in mice. Nat Genet. 1997;17(2):223-5.

36. Truett GE, Heeger P, Mynatt RL, Truett AA, Walker JA, Warman ML. Preparation of PCR-quality mouse genomic DNA with hot sodium hydroxide and tris (HotSHOT). Biotechniques. 2000;29(1):52, 4.
37. Hill CA, Sussan TE, Reeves RH, Richtsmeier JT. Complex contributions of Ets2 to craniofacial and thymus phenotypes of trisomic "Down syndrome" mice. Am J Med Genet A. 2009;149A(10):2158-65.
38. Brown RZ. Social behaviour, reproduction and population changes in the house mouse. Ecol Monogr. 1953;23:217-40.
39. Scattoni ML, Gandhy SU, Ricceri L, Crawley JN. Unusual repertoire of vocalizations in the BTBR T+tf/J mouse model of autism. PLoS One. 2008;3(8):e3067.
40. Scattoni ML, Martire A, Cartocci G, Ferrante A, Ricceri L. Reduced social interaction, behavioural flexibility and BDNF signalling in the BTBR T+ tf/J strain, a mouse model of autism. Behavioural brain research. 2013;251:35-40.
41. Whittemore LA, Song K, Li X, Aghajanian J, Davies M, Girgenrath S, et al. Inhibition of myostatin in adult mice increases skeletal muscle mass and strength. Biochem Biophys Res Commun. 2003;300(4):965-71.
42. Wohr M, Silverman JL, Scattoni ML, Turner SM, Harris MJ, Saxena R, et al. Developmental delays and reduced pup ultrasonic vocalizations but normal sociability in mice lacking the postsynaptic cell adhesion protein neuroligin2. Behavioural brain research. 2013;251:50-64.
43. McFarlane HG, Kusek GK, Yang M, Phoenix JL, Bolivar VJ, Crawley JN. Autism-like behavioral phenotypes in BTBR T+tf/J mice. Genes, brain, and behavior. 2008;7(2):152-63.
44. Yang M, Scattoni ML, Zhodzishsky V, Chen T, Caldwell H, Young WS, et al. Social approach behaviors are similar on conventional versus reverse lighting cycles, and in replications across cohorts, in BTBR T+ tf/J, C57BL/6J, and vasopressin receptor 1B mutant mice. Frontiers in behavioral neuroscience. 2007;1:1.
45. Michetti C, Romano E, Altabella L, Caruso A, Castelluccio P, Bedse G, et al. Mapping pathological phenotypes in reelin mutant mice. Front Pediatr. 2014;2:95.
46. Yang M, Silverman JL, Crawley JN. Automated three-chambered social approach task for mice. Current protocols in neuroscience / editorial board, Jacqueline N Crawley [et al]. 2011;Chapter 8:Unit 8 26.
47. Yang M, Crawley JN. Simple behavioral assessment of mouse olfaction. Current protocols in neuroscience / editorial board, Jacqueline N Crawley [et al]. 2009;Chapter 8:Unit 8 24.
48. Spring S, Lerch JP, Henkelman RM. Sexual dimorphism revealed in the structure of the mouse brain using three-dimensional magnetic resonance imaging. NeuroImage. 2007;35(4):1424-33.
49. Bock NA, Nieman BJ, Bishop JB, Mark Henkelman R. In vivo multiple-mouse MRI at 7 Tesla. Magn Reson Med. 2005;54(5):1311-6.
50. Lerch JP, Sled JG, Henkelman RM. MRI phenotyping of genetically altered mice. Methods Mol Biol. 2011;711:349-61.
51. Dorr AE, Lerch JP, Spring S, Kabani N, Henkelman RM. High resolution three-dimensional brain atlas using an average magnetic resonance image of 40 adult C57Bl/6J mice. NeuroImage. 2008;42(1):60-9.
52. Lerch JP, Carroll JB, Spring S, Bertram LN, Schwab C, Hayden MR, et al. Automated deformation analysis in the YAC128 Huntington disease mouse model. NeuroImage. 2008;39(1):32-9.

53. Nieman BJ, Flenniken AM, Adamson SL, Henkelman RM, Sled JG. Anatomical phenotyping in the brain and skull of a mutant mouse by magnetic resonance imaging and computed tomography. Physiol Genomics. 2006;24(2):154-62.
54. Steadman PE, Ellegood J, Szulc KU, Turnbull DH, Joyner AL, Henkelman RM, et al. Genetic effects on cerebellar structure across mouse models of autism using a magnetic resonance imaging atlas. Autism research : official journal of the International Society for Autism Research. 2014;7(1):124-37.
55. Ullmann JF, Watson C, Janke AL, Kurniawan ND, Reutens DC. A segmentation protocol and MRI atlas of the C57BL/6J mouse neocortex. NeuroImage. 2013;78:196-203.
56. Genovese CR, Lazar NA, Nichols T. Thresholding of statistical maps in functional neuroimaging using the false discovery rate. NeuroImage. 2002;15(4):870-8.

FIGURES

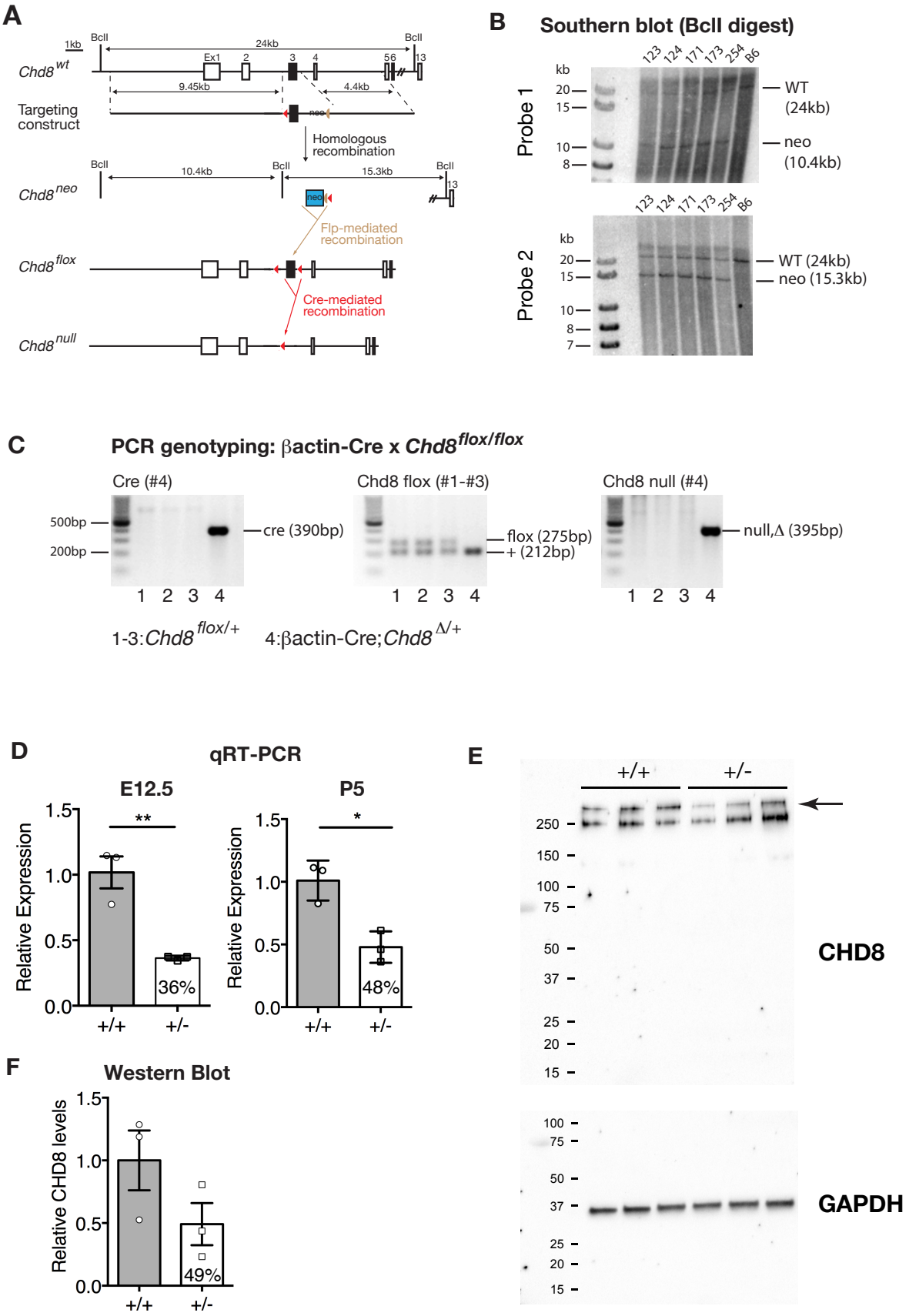
A
1kb
BclI
24kb
BclI
Chd8 wt
Ex1
2
3
4
5 6
13
9.45kb
4.4kb
Targeting construct
neo
Homologous recombination
BclI
10.4kb
BclI
15.3kb
BclI
Chd8 neo
neo
13
Flp-mediated recombination
Chd8 flox
Cre-mediated recombination
Chd8 null
B
Southern blot (BclI digest)
Probe 1
kb
20
15
10
8
123 124 171 173 254 B6
WT (24kb)
neo (10.4kb)
Probe 2
kb
20
15
10
8
7
123 124 171 173 254 B6
WT (24kb)
neo (15.3kb)
C
PCR genotyping: βactin-Cre x Chd8flox/flox
Cre (#4)
500bp
200bp
cre (390bp)
1 2 3 4
Chd8 flox (#1-#3)
flox (275bp)
+ (212bp)
1 2 3 4
Chd8 null (#4)
null,Δ (395bp)
1 2 3 4
1-3:Chd8 flox/+
4:βactin-Cre;Chd8 Δ/+
D
qRT-PCR
E12.5
Relative Expression
1.5
1.0
0.5
0.0
**
36%
+/+
+/-
P5
Relative Expression
1.5
1.0
0.5
0.0
*
48%
+/+
+/-
E
+/+
+/-
250
150
100
75
50
37
25
20
15
CHD8
100
75
50
37
25
20
15
GAPDH
F
Western Blot
Relative CHD8 levels
1.5
1.0
0.5
0.0
49%
+/+
+/-

Supplementary Figure 1. *Chd8* conditional allele.

A) Diagrammatic representations of the wildtype (wt) *Chd8* locus (*Chd8*^{wt}), targeting construct, targeted (neo) allele, conditional (flox) and null alleles. Approximate genomic distances are indicated in kilobases (kb), exons by boxes labelled Ex1 to 13, Southern blot probes (P1,P2) and PCR primers (#1- #4) are indicated. The 5' long homology arm is in red and the 3' short homology arm in green. The neomycin resistance cassette (neo) is shown as a blue box, the floxed exon 3 by a black box, loxP sites by red triangles and frt sites by tan semi-ovals. BclI restriction enzyme sites are labelled.

B) Southern blot of genomic DNA digested with BclI from embryonic stem (ES) cell clones (123, 124 etc.) and wildtype C57BL/6J (B6) cells, hybridised with P1 are shown, with molecular weight markers in the left hand lane. The wildtype allele (WT) gives a 24kb band, whilst the targeted allele gives a band of approximately 10.4kb. Southern blot of genomic DNA digested with BclI from embryonic stem (ES) cell clones as indicated and wildtype B6 cells, hybridised with P2 are shown, with molecular weight markers in the left hand lane. The wildtype allele (WT) gives a 24kb band, whilst the targeted allele gives a band of approximately 15.3kb.

C) PCR genotyping of genomic DNA extracted from mouse pups from a cross between a heterozygous general deleter βactin-Cre transgenic mouse and a *Chd8*$^{flox/flox}$ mouse. Results from PCR reactions to detect the Cre transgene, distinguish the *Chd8*^{flox} and wildtype alleles from each other, and amplify the null allele are shown. Note the loss of the flox allele, with the gain of the null allele in the Cre+ pup.

D) Quantitative RT-PCR for *Chd8* on mRNA extracted from *Chd8* heterozygous mouse neocortices at E12.5 and P5 and littermate controls. *Chd8* expression levels in heterozygous mice are significantly reduced to 36% of wildtype controls at E12.5 ($p=0.006$, $n=3$ per genotype) and 48% at P5 ($p=0.01$, $n=3$ per genotype). $^{*}p<0.05$, $^{**}p<0.01$, student's t-test

E) Western blot on lysates from *Chd8* heterozygous E12.5 neocortices and littermate controls. The arrow shows the 290kDa band for CHD8 that was quantified in F (upper panel). Note the absence of truncated protein products for CHD8. Membranes were then re-probed for the loading control GAPDH (lower panel).

F) Quantification of CHD8 protein levels normalised to GAPDH as shown in E. CHD8 expression in heterozygous mice is 49% compared to wildtype littermates ($p=0.16$, $n=3$ per genotype).

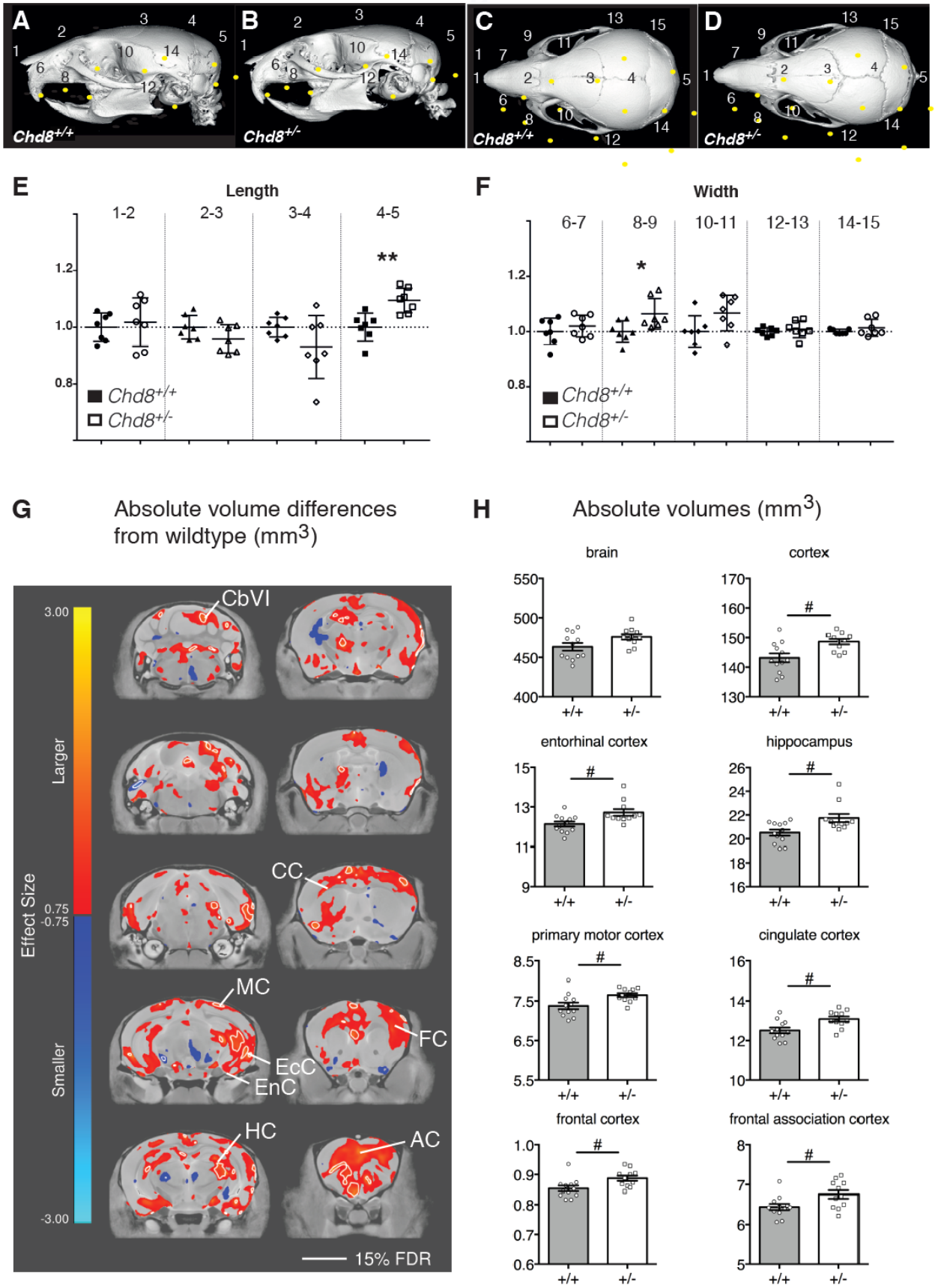
A
B
C
D
Chd8+/+
Chd8+/-
E
Length
1-2
2-3
3-4
4-5
**
F
Width
6-7
8-9
10-11
12-13
14-15
*
G
Absolute volume differences from wildtype (mm3)
Effect Size
Larger
Smaller
3.00
0.75
-0.75
-3.00
CbVI
CC
MC
EcC
EnC
FC
HC
AC
15% FDR
H
Absolute volumes (mm3)
brain
cortex
entorhinal cortex
hippocampus
primary motor cortex
cingulate cortex
frontal cortex
frontal association cortex
+/+
+/-

Figure 1. Hypertelorism and mild megalencephaly in *Chd8*$^{+/-}$ mice.

A-D) Representative lateral (A,B) and dorsal (C,D) μCT views of 3D reconstructed skulls from mice with the indicated genotypes. Landmarks from 1 to 15 are indicated by yellow dots. Scale bars = 2mm.

E,F) Graphs for measurements between indicated landmarks, normalised to average measurements from corresponding wildtype littermates. Mean±SEM; *$p \leq 0.05$, **$p \leq 0.01$, student's t-test.

G) High-resolution 7T structural MRI coronal images of *Chd8*$^{+/-}$ brains (from mice assessed for behaviours, Figure 2), from posterior (top left) to anterior (bottom right) are shown. Absolute volumetric differences in size, relative to wildtype controls are coloured according to the scale on the left. Effect size is measured in units of standard deviation. Some regions with enlarged volumes are labelled as follows: CbVI – cerebellar lobule VI, MC – motor cortex, EcC – ectorhinal cortex, EnC – entorhinal cortex, HC – hippocampus, CC - Cingulate cortex, FC – frontal association cortex, AC – anterior commissure

H) Absolute volumes (mm^3) are plotted for whole brain, neocortex and several other brain regions for the different genotypes as indicated. #FDR<0.15, *Chd8*$^{+/-}$: n=11, *Chd8*$^{+/+}$: n=12

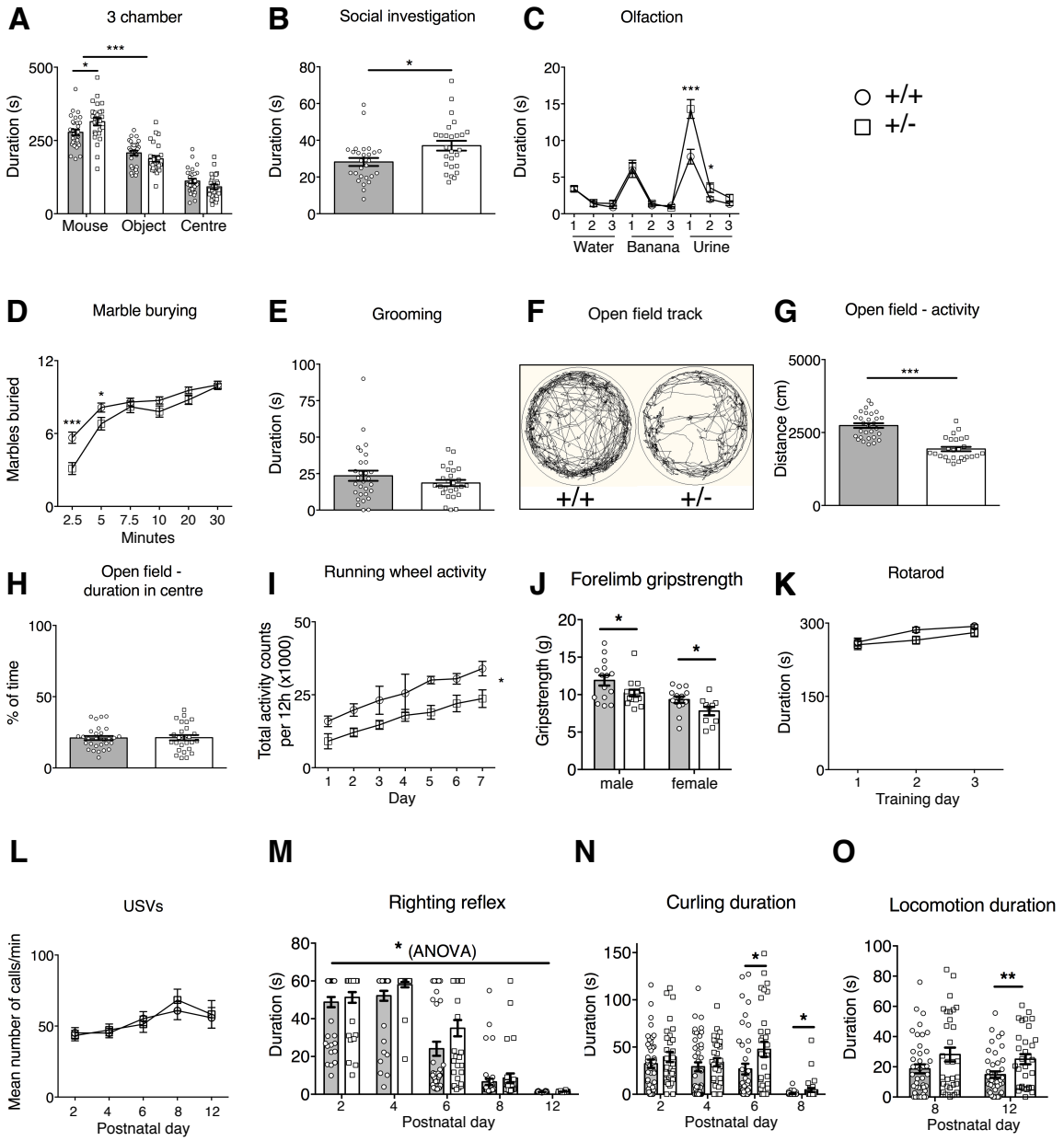

Figure 2. Complex behavioural abnormalities in *Chd8* heterozygous mice.
A-O) Behavioural assessments of a cohort of adult *Chd8*$^{+/-}$ (+/-, n=26) and *Chd8*$^{+/+}$ (+/+, n=29) and of pup *Chd8*$^{+/-}$ (+/-, n=32) and *Chd8*$^{+/+}$ (+/+, n=42) animals.

A) The duration, in seconds, spent in each chamber of the three-chamber sociability test. All mice spent a significantly higher proportion of time in the chamber with the age- and sex-matched stranger con-specific mouse compared to the other chambers. Mean±SEM; *p≤0.05, ***p≤0.0001 (between-subjects ANOVA with student's t-test as post-hoc analysis).
B) Duration, in seconds, of social investigation over a three-minute period. Social investigation was defined as the combined total duration of head, body and anogenital sniffing of a conspecific mouse. Mean ±SEM; *p≤0.05 (between-subjects ANOVA with student's t-test as post-hoc analysis).

C) Graph demonstrating the performance in the olfactory habituation/dishabituation test. Mean±SEM; *p≤0.05, **p≤0.0002 (repeated-measures ANOVA with student's t-test as post-hoc analysis).
D) The average number of marbles buried, out of a maximum of 12, within a 30-minute time period. Mean±SEM; *p≤0.05, ***p≤0.0005 (repeated-measures ANOVA with student's t-test as post-hoc analysis).
E) The duration, in seconds, mice spent self-grooming during the 10-minute self-grooming test. Mean±SEM (between-subjects ANOVA).
F) Representative ethovision tracks of a *Chd8*$^{+/-}$ (+/-) and *Chd8*$^{+/+}$ (+/+) animal plotting their movements during the 10-minute open field task.
G) The total distance travelled in the outer part of the open field arena over a 10-minute time-period. Mean±SEM; ***p<0.0001 (between-subjects ANOVA).
H) The percentage of time spent in the centre of the open field arena during the 10-minute test. Mean±SEM (between-subjects ANOVA).
I) The total activity counts per 12h period on running wheels in the homecage during 7 days of dark-phase recording. Mean±SEM; *p<0.05 (repeated-measures ANOVA).
J) The average of 3 measurements of forelimb grip strength on a Linton Grip Strength meter. Error bars indicate Mean ± SEM, *p<0.05
K) The mean latency of mice to fall from the rotarod. Mean±SEM (repeated-measures ANOVA).
L) The mean number of ultrasonic vocalisations per minute on indicated postnatal days. Mean±SEM (repeated-measures ANOVA).
M) The development of the righting reflex in pups at the indicated postnatal days. Note the significant delay in the acquisition of the full righting reflex response in *Chd8*$^{+/-}$ animals compared to littermate controls (one-way repeated-measures ANOVA: F(1,72)=6.36, p=0.014, with student's t-test as post-hoc analysis). Mean ±1SEM; *p≤0.05.
N) The duration, in seconds, pups spend rolling on their back (curling) as recorded during the analysis of spontaneous movements during USV recordings. Note that *Chd8*$^{+/-}$ mice spent significantly more time curling at P6 and P8 compared to littermate controls (one-way repeated-measures ANOVA: F(1,72)=12.64, p=0.001, with student's t-test as post-hoc analysis). Mean ± SEM; *p≤0.05.
O) The duration, in seconds, pups spend in locomotion as recorded during the analysis of spontaneous movements during USV recordings. At P12 *Chd8*$^{+/-}$ animals spent significantly more time in locomotion as compared to littermate controls (one-way repeated measures ANOVA: (F(1,72)=7.33, p=0.008, with student's t-test as post-hoc analysis). Mean ±1SEM, **p≤0.005.

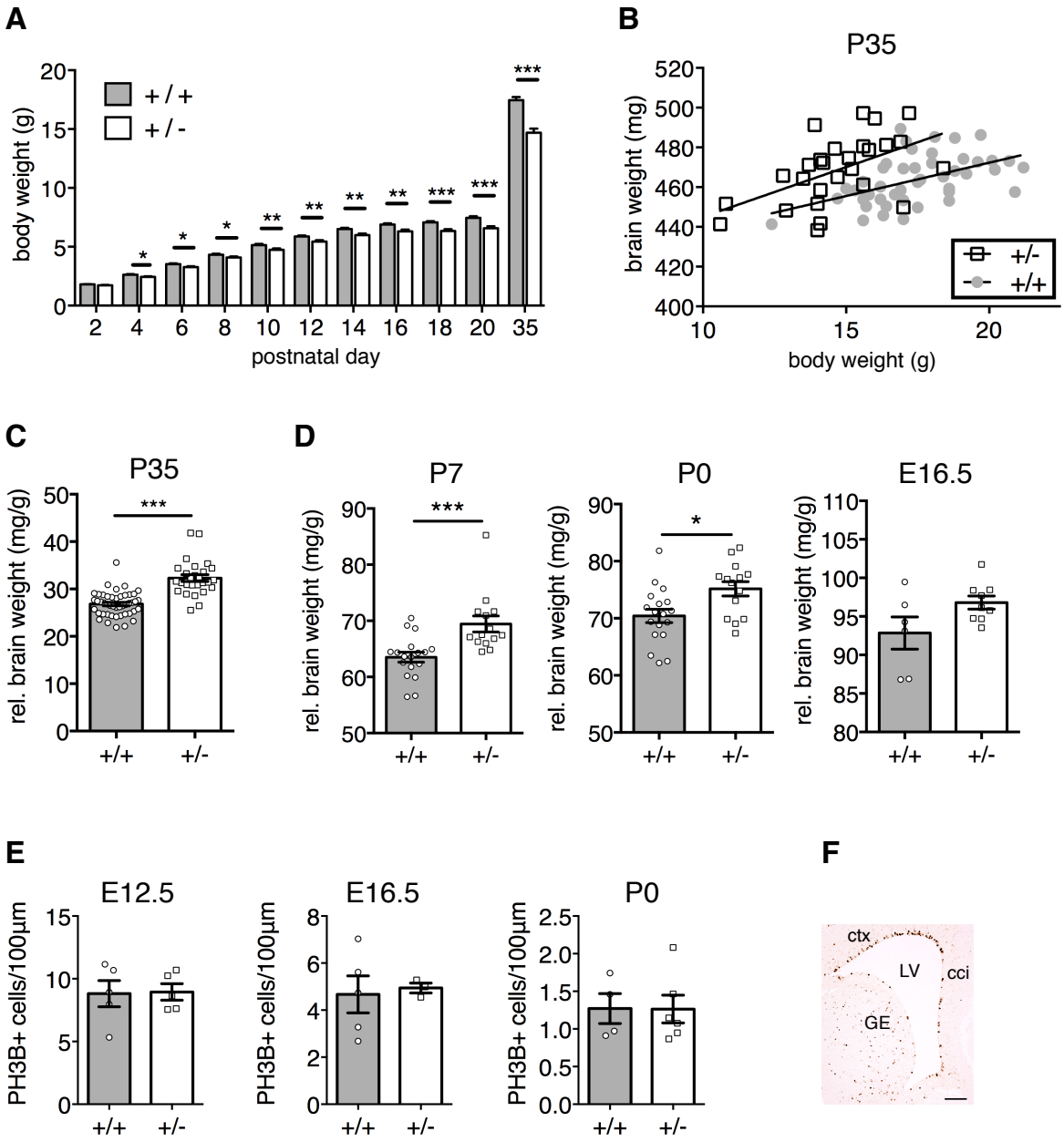

Figure 3. *Chd8* mutants display postnatal brain hypertrophy.
A) Body weights of mice between P2 and P35. Repeated-measures ANOVA with student's t-test as post hoc analysis. *p<0.05, **p<0.01, ***p<0.001
B) Individual brain wet weights plotted against individual body weights for *Chd8*$^{+/-}$ (+/-), mice and their littermate controls (+/+) at postnatal day (P)35. Note that *Chd8*$^{+/-}$ mice have larger brain weights than littermate controls of equivalent body weight.
C) Brain wet weights normalised to body weight P35. *Chd8*$^{+/-}$ (+/-) show significantly increased normalised brain weights compared to their littermate controls (+/+). Mean ± SEM; **p<0.01; ***p<0.001 (student's t-test). +/+, n=46; +/-, n=27; +/+,
D) Brain wet weights of pups at P7, P0 and embryonic day (E)16.5 normalised to body weight. *Chd8*$^{+/-}$ (+/-) pups show significantly larger normalized brain weights than their littermate controls (+/+) at P7 and P0. Mean ± SEM; *p<0.05, ***p<0.001 (student's t-test). P7: +/+, n=18; +/-, n=14; +/+; P0: +/+, n=18; +/-, n=14; +/+; E16.5: +/+, n=6; +/-, n=9.

E) Quantification of phospho-histone H3 (PH3B) positive cells in the ventricular zone at embryonic day E12.5, E16.5 and P0. Cell counts were normalized to ventricular surface length. Mean ± SEM; student's t-test. E12.5: +/+, n=5; +/-, n=5. E16.5: +/+, n=5; +/-, n=3. P0: +/+, n=4; +/-, n=6.
F) Example of PH3B immunostaining in an embryonic day E16.5 coronal brain section. Scale bar = 100µm; LV: lateral ventricle, ctx: cortex, cci: cingulate cortex, GE: ganglionic eminence.

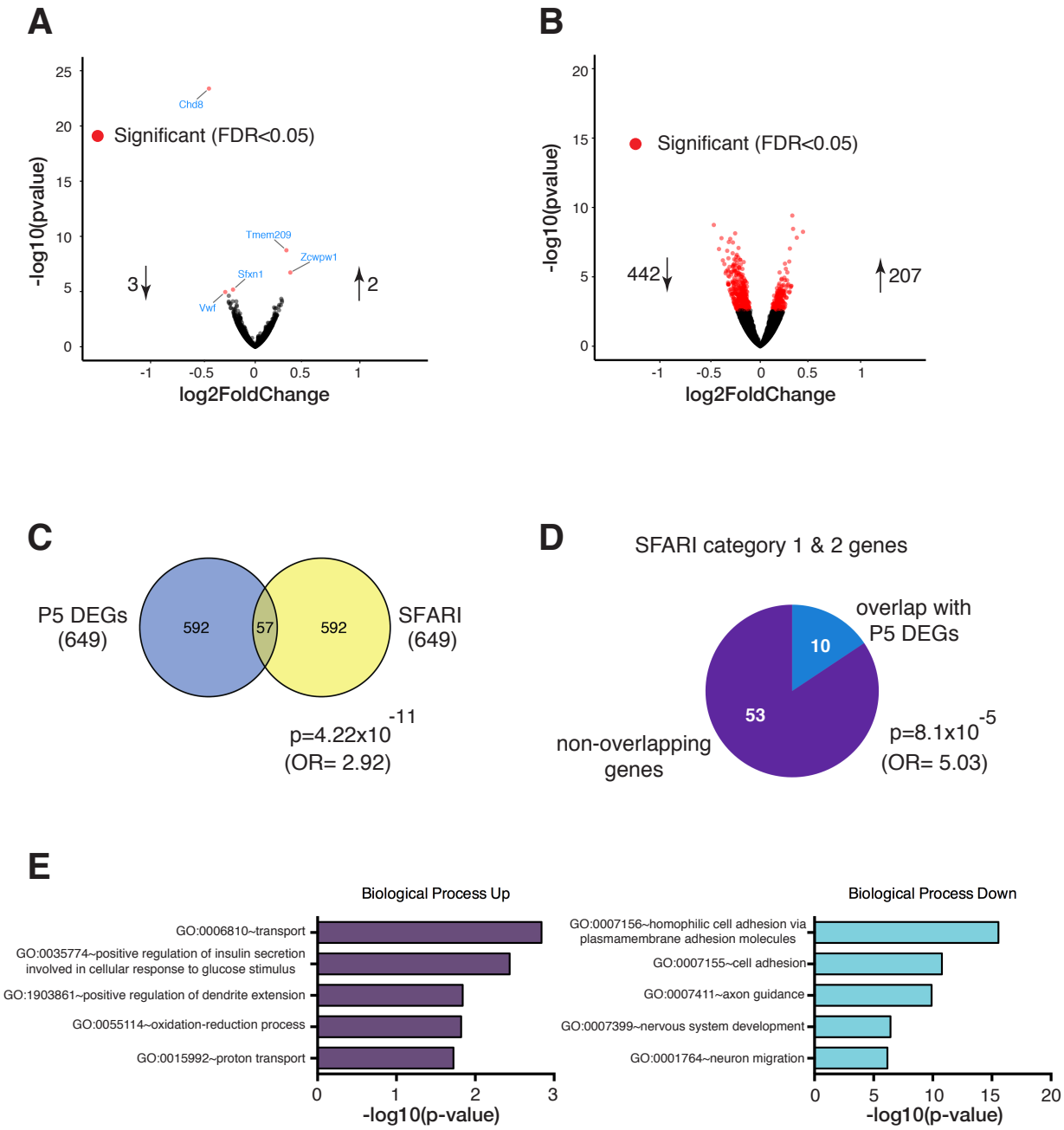

Figure 4. Gene expression changes in *Chd8*-deficient neocortices.
A) Volcano plot indicating all DEGs detected by RNA-seq in E12.5 *Chd8*$^{+/-}$ embryonic cortex. Each point represents an individual gene and all heterozygote DEGs detected using an FDR of 0.05 are highlighted in red.
B) Volcano plot indicating all DEGs detected by RNA-seq in P5 *Chd8*$^{+/-}$ embryonic cortex.
C) Venn diagram showing extent of overlap between P5 DEGs and ASD associated genes (categories 1-5 & S) in the SFARI gene database.
D) Pie chart showing the proportion of high confidence ASD candidate genes (categories 1-2) that are found in the P5 DEG set.
E) DEGs (FDR < 0.05) were screened for Gene Ontology terms in Biological Processes using the DAVID knowledgebase. The five most significant terms are shown for up-regulated DEGs (left panel) and down-regulated DEGs (right panel), respectively.

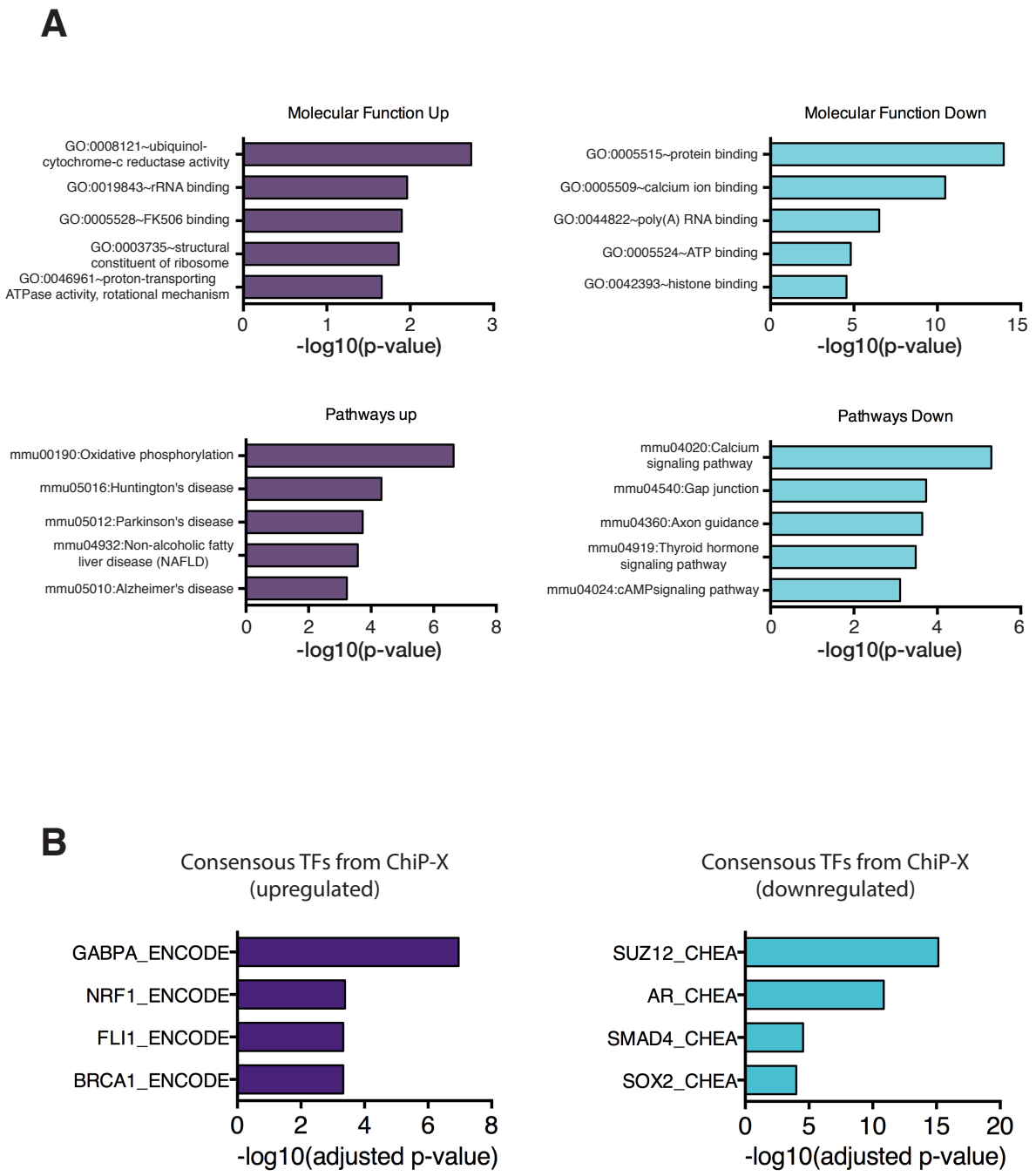

Supplementary Figure 2: Functional Enrichment Analysis of differentially expressed genes (DEGs) in P5 embryos.

A) DEGs (FDR < 0.05) were screened for Gene Ontology terms in the Molecular Function category (Top Panels) and subjected to KEGG pathway enrichment (Bottom Panels) using the DAVID knowledgebase. The five most significant terms are shown for up-regulated DEGs (left panels) and down-regulated DEGs (right panels), respectively.

B) DEGs (FDR < 0.05) were subjected to enrichment analysis using the "ENCODE and ChEA Consensus TFs from ChIP-X" database on Enrichr, to identify putative upstream regulatory transcription factors. The four most overrepresented transcription factors are shown for up-regulated (left) and down-regulated (right) DEGs, respectively.

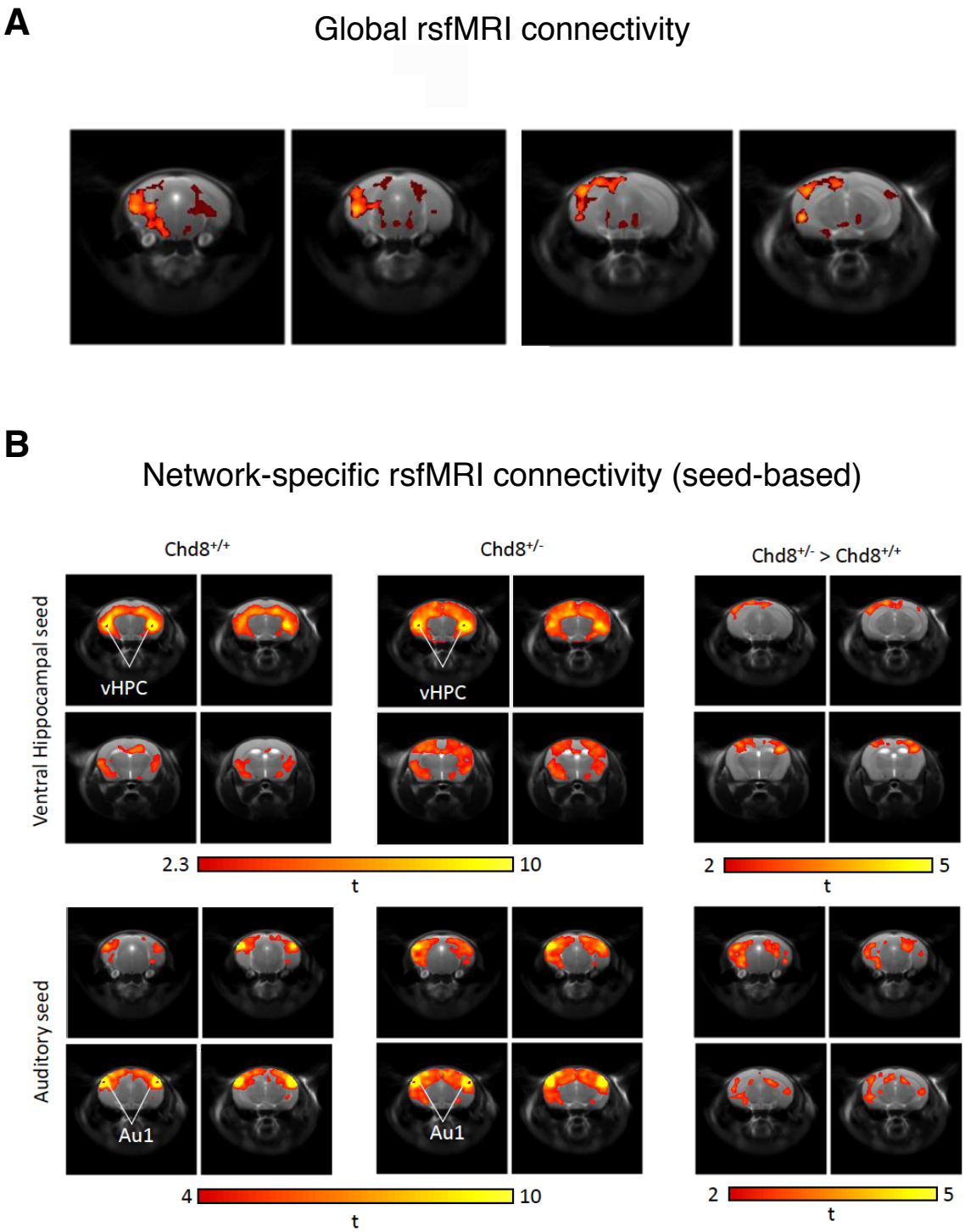

Fig. 5: Resting state function MRI reveals connectivity changes in *Chd8*$^{+/-}$ mice
A) Foci of reduced long-range connectivity in *Chd8*$^{+/-}$ versus wildtype control littermates
B) Seed-correlation mapping highlighted increased connectivity between the ventral hippocampus (vHPC) and cortical areas (top panels) as well as between the auditory cortex (Au1) and parietal cortical areas and hippocampus.

Chd8$^{+/-}$: n=19, *Chd8*$^{+/+}$: n=23

Supplementary information:

Supplementary Table 1. Absolute volumetric differences in specific brain regions between *Chd8*$^{+/-}$ and *Chd8*$^{+/+}$ mice as determined by MRI.

Supplementary Table 2. Differentially expressed genes in E12.5 *Chd8*$^{+/-}$ embryos compared to wildtype controls.

Supplementary Table 3. Differentially expressed genes in P5 *Chd8*$^{+/-}$embryos compared to wildtype controls.

Supplementary Table 4. SFARI ASD genes overlapping with P5 differentially expressed genes.

Supplementary Table 5. Up-regulated Gene Ontology: Biological Processes

Supplementary Table 6. Down-regulated Gene Ontology: Biological Processes

Supplementary Table 7. Up-regulated Gene Ontology: Molecular Function

Supplementary Table 8. Down-regulated Gene Ontology: Molecular Function

Supplementary Table 9. Up-regulated Gene Ontology: Pathways

Supplementary Table 10. Down-regulated Gene Ontology: Pathways